First Direct Measurement of T-violation

Mats Danielsson

KUNGLIGA TEKNISKA HÖGSKOLAN
Stockholm 1996

my teacher and
source of inspiration
in experimental
physics

Herzliche Grüße

Mats

First Direct Measurement of T-violation

Mats Danielsson

AKADEMISK AVHANDLING

som med tillstånd av Kungliga Tekniska Högskolan framlägges till offentlig granskning för vinnande av teknologie doktorsexamen
fredagen den 16 februari 1996, kl. 10^{15}
i föreläsningssalen, Manne Siegbahnhuset, KTH Frescati
Frescativägen 24, Stockholm

Avhandlingen försvaras på engelska

Kungliga Tekniska Högskolan
Stockholm 1996

Mats Danielsson: First Direct Measurement of T-Violation

ABSTRACT

The unique features of the CPLEAR experiment at CERN that enable a tagging of the strangeness of neutral kaons are used to detect a difference between the transition rate of $K^0 \rightarrow \overline{K^0}$ and $\overline{K^0} \rightarrow K^0$. These processes are each others time inverse and by measuring the difference a direct measurement of T-violation is made for the first time in particle physics. The measured value for the asymmetry is $(8.6 \pm 2.2_{stat} \pm 1.0_{sys})10^{-3}$. The results do not reveal any evidence for a violation of the CPT symmetry.

Descriptors: CPLEAR, CPT, C_6F_{14}, Cherenkov radiator, T-violation, symmetry, ultrasound

ISBN 91-7170-738-7
Akademitryck AB Edsbruk 1996

Till Maria

Contents

Chapter 1

Introduction

The existence of symmetries is indicated by selection rules and conservation laws. The symmetries can be discrete or continuous, global or local and they can be exact or violated. C, P and T [1] are examples of discrete symmetries, which as far as we know today, are exact in strong and electromagnetic interactions while C and P are maximally violated in weak interactions. According to Noether's theorem [1] there is a symmetry behind every conservation law, e.g. translational symmetry implies conservation of linear momentum. Ultimately symmetries determine the laws of nature.

The aim of the CPLEAR[2] [2, 3] experiment at CERN is to study the symmetries C,P and T through decays of neutral kaons into different final states.

[1] see chapter 3 for definitions of C, P and T

[2] Univ. Athens, Univ. Basle, Univ. Boston, CERN, Univ. Coimbra, Delft Tech. Univ., Demokritos IPN, Univ. Fribourg, Univ. Ioannina, Univ. Liverpool, Univ. Lubljana, CPPM Marseille, PSI Villigen, CEN DPhPE Saclay, KTH Stockholm, Univ. Thessaloniki and ETH Zürich

1.1 Brief history

Until 1957 it was taken for granted that all interactions were invariant under the symmetries C, P and T and any combination of them. When Lee and Yang [4], considering decays of K-mesons, proposed that Parity might be violated in weak interactions and then this was shown experimentally to be the case [5], it was one of the most surprising and non-intuitive results in modern physics this century. The fact that it is possible through experiments to distinguish the two possible definitions of left and right is indeed extraordinary.

Subsequently it was generally assumed that C and P are individually maximally violated in weak interaction while the combination of CP would still be a good symmetry. When Christenson, Cronin, Fitch and Turlay in 1964 tried to improve the limits on possible CP-violation it was not considered as a very hot subject and they got only parasitic beam time at the Brookhaven accelerator [6]. In spite of this they detected CP forbidden decays of the long lived kaon (K_L) into two pions at the level of 0.2% [7]. Other experiments also measured a charge asymmetry [8] in the semileptonic decays of K_L which gave further evidence of CP-violation.

Ever since these measurements the assumption has been that CP and T are violated to the same extent in weak interaction and so CPT remains a good symmetry. More generally the CPT theorem [9, 10, 11] states that a Lorentz invariant local quantum field theory is invariant under any combination of the operators CPT. This invariance implies e.g. that the masses and lifetimes of particle and antiparticle pairs are identical. There is thus strong theoretical prejudice against a violation of CPT. In quantum field theories for gravity it is, however, questioned [12, 13, 14] and in spite of a lack of theories which are not CPT invariant, this invariance should be subject to experimental checks.

The assumed T-violation in the neutral kaon system has never been directly measured but only deduced assuming CPT and/or unitarity. CPT requires that CP is violated to the same extent in K_L and in the short lived kaon (K_S). This has never been experimentally verified.

In spite of 30 years of intense experimental efforts, several parameters describing the kaon system have still not been measured and the origin

of CP violation is unknown. Almost as many questions as in 1970 remain unanswered. For general reviews of CP-violation see e.g. Ref. [15, 16, 17].

1.2 Origin of CP violation

The origin of the CP-violation has been under much debate. With three quark families there is a phase in the CKM matrix[3] that cannot be eliminated and this introduces CP-violation into the Standard Model in an elegant and natural way [18]. When this was first suggested [19] neither the charm, bottom nor the top quark had been found.

There are several other proposed explanations for CP-violation: The most famous one is Wolfenstein's so called super weak $\Delta S = 2$ interaction [20], although, perhaps, the most spectacular one considers CP violation to be induced by antigravity [21]. One possible way of separating the Standard Model theory from, for example, the superweak model is that the Standard Model not only predicts a CP violation in the mixing of the kaons ($\Delta S = 2$) but also in the decay ($\Delta S = 1$). CP violation in the decay is referred to as direct CP-violation[4] and its measurement has been (and still is) the main goal of several experiments [22, 23, 24, 25, 26]. The difficulty in measuring the direct CP violation ϵ' is its smallness: its contribution to the total CP violation ϵ is less than 0.2% of the contribution from the mixing. Using the recently measured mass of the top quark $(176 \pm 13) GeV$ [27] the standard model prediction for ϵ'/ϵ has decreased to the order $5 \cdot 10^{-4}$ [28]. The accuracy and statistics required to measure a value of ϵ'/ϵ significant from zero is out of reach for CPLEAR, even though this was the original intention when the experiment was first proposed in 1985. In order to conclusively test the standard model concerning CP-violation one may have to go to the B-system, where the theoretical uncertainties in the predictions are significantly smaller. Several dedicated experiments are under way at the B-factories under construction and also at the HERA accelerator at DESY as well as at the next CERN accelerator LHC.

[3]The CKM matrix [19] determines the amplitude of the charged current weak interactions between the u, d, s, c, b and t quarks.

[4]The concept of direct CP-violation is not connected to the concept of a direct measurement of T-violation. The meaning of "direct" in the latter case is only that the interpretation of the measurement is straight forward.

1.3 Tests of CPT symmetry

In searching of CPT violation one could compare the masses or decay times of any particle anti-particle pair, such as proton-antiproton or electron-positron. Since there is no theory that is not CPT invariant, there is no clearly defined place where one expects to find a CPT violation. There are, however, some reasons to concentrate the search in the kaon system or other similar systems. One reason is that due to the interference between the K_L and the K_S it is possible to measure any difference in mass between K^0 and $\overline{K^0}$ with an accuracy almost ten orders of magnitude better than in any other case [29]. Another reason is that the kaon system is the only place were CP-violation has been observed.

1.4 The CPLEAR experiment

The usual approach of neutral kaon experiments is to create the kaons with high energy protons incident on a fixed target [22, 23]. These experiments have in common that the $K^0/\overline{K^0}$ content of the beam is not known.

In CPLEAR the kaons are produced in annihilations at rest through the reaction $p\bar{p} \rightarrow K^{\pm}\pi^{\mp}\overline{K^0}(K^0)$. This annihilation channel will be referred to as the golden channel. The unique feature is that it tags the $K^0(\overline{K^0})$ through the charge of the accompanying $K^-(K^+)$, i.e. the initial strangeness is known. Through the $\Delta S = \Delta Q$ rule one also knows the strangeness when a semileptonic decay $(K^0(\overline{K^0}) \rightarrow \pi^{\pm}e^{\mp}\nu)$ takes place and this opens up the possibility of measuring the strangeness content of the neutral kaons as a function of time.

The goal of this thesis is to use this unique feature of CPLEAR to directly test the CPT and T symmetries. Most exciting it would of course have been to measure a deviation from the CPT symmetry. The result is, however, consistent with CPT and the measured T-violation is in agreement with what we expect assuming CPT.

1.5 Outline of the thesis

In chapter 2 an overview of the phenomenology of neutral kaons and measurable quantities in CPLEAR is given. In chapter 3 the CPLEAR detector is described while chapter 4 is dedicated to the ultrasonic treatment of the C_6F_{14} liquid Cherenkov radiator. The analysis and the results obtained for semileptonic decays of neutral kaons is finally presented in chapter 5-7.

1.6 Author's contribution

When I joined the CPLEAR collaboration and started to work on my PhD the CPLEAR detector was already designed and most detector parts had been constructed. My contribution to the hardware of CPLEAR has thus been to assemble and test the detector and to help solving unforeseen problems mainly with the C_6F_{14} Cherenkov liquid and also with PM-tubes, electronics etc.

In the first 1.5 years with CPLEAR I worked at CERN mounting the Particle Identification Detector and testing each of the 32 sectors using cosmic rays. In 1992 they were installed in the detector and a one week run was made over Easter 1992 to test the general performance of the detector.

After this I worked intensively on solving problems connected with dissolved gases in the C_6F_{14} liquid Cherenkov radiator before the main data taking started in the beginning of August 1992. Together with H.-J. Gerber I did a major part of the work of designing, testing and successfully implementing a system based on the use of ultrasound to drive out the gases. The highest priority was put into this work since the functionality of the Cherenkov counters is crucial for the experiment.

During our data taking periods I was responsible for monitoring the detector performance and checking the data quality during some 50 shifts. I have also helped to improve the Monte Carlo detector simulation program. The analysis presented in this thesis has, if not otherwise explicitly stated, been done by myself.

In the end there is also a list of papers covering areas of my work that I have chosen not to include in this thesis.

Chapter 2

Phenomenology of the neutral kaon system

The purpose of this chapter is to give an overview of the phenomenology of the neutral kaon system and to discuss the significance of a direct measurement of T-violation. For this we have used results in [30, 31, 32, 33]. The symmetries C, P and T are introduced in the first section. The matrix governing the neutral kaon system is given in section 2.2 and the measurable quantities are expressed in the matrix elements. In section 2.3 the measurement of T-violation is discuss and section 2.4 contains a parameterization of possible violations of the T and CPT symmetries. The following section 2.5 deals with an investigation of the predicted CPT- and/or T-violation in the neutral kaon system assuming unitarity. In the last section the different forms of measured asymmetries in CPLEAR are given.

2.1 The discrete symmetries C, P and T

The discrete symmetries C, P and T are defined in the following ways. The operator $\check{C}$ changes particles to their antiparticles. Particles like the photon, which is its own antiparticle, are not changed at all. $\check{P}$ reflects all spatial coordinates about the origin, i.e. x to $-x$, y to -y and z to

$-z$. The eigenvalue of $\check{P}$ and $\check{C}$ for a system of particles is determined by the product of the internal particle eigenvalues and the eigenvalues of the wave function ψ describing the motion. The internal $\check{P}$ and $\check{C}$ eigenvalues are the eigenvalues for the particle at rest.

The classical $\check{T}$ operator changes the time variable from t to $-t$. This means reversing kinematical variables like linear and angular momentum. In quantum mechanics t is not an operator but a parameter. This makes the $\check{T}$ operator different from $\check{P}$ and $\check{C}$. The $\check{T}$ operator should in quantum mechanics be defined [34] according to the correspondence principle, in such a way that it is in agreement with classical motion reversal. It must also be consistent with the commutation relations determining the kinematics in quantum mechanics. For example for linear momentum $\check{P}$ and position $\check{X}$ the commutation relation

$$[\check{P}_j, \check{X}_k] = -i\hbar\delta_{jk} \tag{2.1}$$

must be preserved. The fact that $\check{T}$ reverses motion leads to:

$$[\check{T}\check{P}_j\check{T}^{-1}, \check{T}\check{X}_k\check{T}^{-1}] = -[\check{P}_j, \check{X}_k] \tag{2.2}$$

Comparing eq. (2.1) and eq. (2.2) gives

$$\check{T}i\check{T}^{-1} = -i \tag{2.3}$$

and therefore $\check{T}$ must include the operation $\check{K}$ of complex conjugation. The operator $\check{T}$ can generally be written as $\check{U}\check{K}$ where $\check{U}$ is a unitary operator for the set of kinematic variables defining the Hilbert space for the system. With this definition of the $\check{T}$ operator, and, if all interactions vanish, the Schrödinger equation

$$i\hbar\frac{\partial \mid \psi >}{\partial t} = H_0 \mid \psi > \tag{2.4}$$

is left invariant under $\check{T}$.

The $\check{T}$ operator [35] is involutional, i.e. if repeated twice it is equal to the identity operator multiplied with a phase factor. It is also anti unitary.

2.2 The neutral kaon system

The $K^0 - \overline{K^0}$ mesons, discovered by Rochester and Butler 1947 [36], provide a rare situation in the sense that no conservation law forbids transformation from particle to antiparticle and vice versa via intermediate states such as $\pi^+\pi^-$ [37]. This happens only for very few particles and it seems that measurements of the same kind as for the $K^0 - \overline{K^0}$ can only be made for B mesons. Because of the (almost) CP invariant weak interaction governing the mixing of the $K^0 - \overline{K^0}$ system the observable physical eigenstates (denoted K_S and K_L), that are linear combinations of the $K^0 - \overline{K^0}$ states, will be close to eigenstates of CP. The wave functions of the K_S and K_L will interfere with each other and this interference enables very precise measurements on the $K^0 - \overline{K^0}$ system.

The non-relativistic decay formalism [38] [39] of an unstable degenerate state gives:

$$i\hbar \frac{\partial \mid \psi(t) >}{\partial t} = R \mid \psi(t) > \tag{2.5}$$

The Hamiltonian $\mathbf{R}$, which governs the kaon system, can be written as

$$\mathbf{R} = \mathbf{H_0} + \mathbf{H} \tag{2.6}$$

where $\mathbf{H_0}$ contains the electromagnetic and strong interactions and $\mathbf{H}$ the weak interaction. The weak interaction can be further split:

$$\mathbf{H} = \mathbf{M} - \frac{i}{2}\mathbf{\Gamma} \tag{2.7}$$

The $\mathbf{M}$ matrix describes the mixing of the K^0 and $\overline{K^0}$ and $\mathbf{\Gamma}$ describes the decay. Neglecting higher orders of $\mathbf{H}$ and weak interactions between the final states it is possible to express the four matrix elements of $\mathbf{M}$ as

$$M_{\alpha\beta} = m_K \delta_{\alpha\beta} + < \alpha \mid H \mid \beta > + P \sum_{k=1}^{n} \frac{< \alpha \mid H \mid k >< k \mid H \mid \beta >}{(E_k - m_K)}) \tag{2.8}$$

for all different virtual and real states k where E_k is the energy of the state and m_K is the rest energy of the $K^0(\overline{K^0})$. P denotes the Cauchy principal value of the integral. All virtual and real transitions between K^0

and $\overline{K^0}$ are included in the mixing matrix M. The four matrix elements of Γ are

$$\Gamma_{\alpha\beta} = 2\pi \sum_{k=1}^{n} < \alpha \mid H \mid k >< k \mid H \mid \beta > \delta(E_k - m_K) \tag{2.9}$$

for all different final states k. Note that the matrix elements of M and Γ are evaluated in the rest frame of the neutral $K^0(\overline{K^0})$ at the energy corresponding to the neutral kaon mass.

The eigenvalues λ_i of $\mathbf{H}$ are

$$\lambda_S = m_S - i\gamma_S/2 \tag{2.10}$$

and

$$\lambda_L = m_L - i\gamma_L/2 \tag{2.11}$$

where $m_{S,L}$ and $\gamma_{S,L}$ are the masses and widths of the physical states K_S and K_L.

Inversely one can write measurable quantities in terms of the elements of the Hamiltonian $\mathbf{H}$. Of the eight different quantities in the matrix $\mathbf{H}$ only seven of them are measurable since the phase between K^0 and $\overline{K^0}$ is arbitrary. These quantities are:

- mean kaon mass (real number, hermiticity assumed):

$$m_K = (M_{11} + M_{22})/2 = Re(H_{11} + H_{22})/2 \tag{2.12}$$

- mean kaon decay width (real number, hermiticity assumed):

$$\gamma_K = (\Gamma_{11} + \Gamma_{22})/2 = -Im(H_{11} + H_{22}) \tag{2.13}$$

- mass difference Δm between K_L and K_S (real number, hermiticity assumed):

$$\Delta m = Re(\sqrt{4H_{12}H_{21} + (H_{22} - H_{11})^2}) \tag{2.14}$$

- difference in decay width between K_L and K_S (real number, hermiticity assumed):

$$\Delta\gamma = -2Im(\sqrt{4H_{12}H_{21} + (H_{22} - H_{11})^2}) \tag{2.15}$$

- CPT violating parameter (complex number, hermiticity not assumed):

$$\theta = \frac{H_{22} - H_{11}}{\Delta\lambda} \tag{2.16}$$

- T violating parameter (real number, hermiticity not assumed):

$$\chi = \frac{|H_{12}|^2 - |H_{21}|^2}{|H_{12}|^2 + |H_{21}|^2} \tag{2.17}$$

For an operator hermiticity requires $W^\dagger = W$ and thus $M_{21} = M_{21}^*$, $\Gamma_{21} = \Gamma_{21}^*$ and all diagonal elements to be real.

2.3 Measurement of T-violation

A test of T invariance might be hard to imagine since one cannot reverse time. One can, however, imagine what would happen if time was reversed by considering motion reversal. If the Hamiltonian $\check{H}$ governing a system is T invariant it commutes with the T operator. Thus T invariance requires that $H_{12} = H_{21}$ within a phase factor while there is no constraint on H_{11} and H_{22}.

The difference of the rates $|< K^0 \mid H \mid \overline{K^0} >|^2$ and $<| \overline{K^0} \mid H \mid K^0 >|^2$ is the difference between a process and its time reversed process. These rates are measured in CPLEAR and any difference significant from zero is a direct measurement of the T-violation.

2.4 Parameterization of possible T and/or CPT violation

From now on the arbitrary phase between $\mid K^0 >$ and $\mid \overline{K^0} >$ is chosen according to $CP \mid K^0 >= \overline{K^0}$. Applying perturbation theory to the Schrödinger equation and allowing for possible T and/or CPT violation the following expressions (not normalized) for the eigenfunctions $|K_S >$ and $|K_L >$ are obtained.

$$|K_S >= \left[(1 + \epsilon_T + \delta_{CPT})|K^0 > +(1 + \epsilon_T - \delta_{CPT})|\overline{K^0} >\right] \tag{2.18}$$

$$|K_L>=\left[(1+\epsilon_T-\delta_{CPT})|K^0>-(1+\epsilon_T+\delta_{CPT})|\overline{K^0}>\right] \quad (2.19)$$

where ϵ_T parameterizes the T-violation while δ_{CPT} parameterizes the CPT violation. $Re(\epsilon_T)$ and δ_{CPT} correspond to $\chi/4$ in eq. (2.17) and $\theta/2$ in eq. (2.16) respectively. The former parameters are more commonly used in the literature. The $\mid K_S >$ and $\mid K_L >$ observable states are related to the pure CP eigenstates (not normalized) as

$$|K_S>=|K_1>+\epsilon_S|K_2> \quad (2.20)$$

$$|K_L>=\epsilon_L|K_1>+|K_2> \quad (2.21)$$

where ϵ_S and ϵ_L are small admixtures of the "wrong" CP eigenstate. The CP violation parameters ϵ_S and ϵ_L are connected to the T and CPT violation parameters ϵ_T and δ_{CPT} through the relations:

$$\epsilon_T=\frac{\epsilon_S+\epsilon_L}{2} \quad (2.22)$$

$$\delta_{CPT}=\frac{\epsilon_S-\epsilon_L}{2} \quad (2.23)$$

2.5 The Bell-Steinberger Relation

Using the unitarity relation it is possible to check the consistency of a CPT invariant description of the kaon system. Consider an initial state according to

$$|\psi>=ae^{-i\lambda_S t}|K_S>+be^{-i\lambda_L t}|K_L> \quad (2.24)$$

The total transition rate[1]

$$\sum_{k=1}^{n}\mid a<k\mid T\mid K_S>+b<k\mid T\mid K_L>\mid^2 \quad (2.25)$$

must equal the derivative of the norm

$$\begin{aligned}\psi\psi^\dagger=&\mid a\mid^2 e^{-\gamma_S t}+\mid b\mid^2 e^{-\gamma_L t}+\\ &b^*ae^{i(\lambda_L^*-\lambda_S)t}<K_L\mid K_S>+\\ &a^*be^{i(\lambda_S^*-\lambda_L)t}<K_S\mid K_L>\end{aligned} \quad (2.26)$$

[1]In this section T is the transition operator

at all times and for all a and b. At the time t=0 we have

$$-\frac{d}{dt}\psi\psi^{\dagger} = \gamma_S \mid a \mid^2 + \gamma_L \mid b \mid^2 - \\ ib^*a(\lambda_L^* - \lambda_S) < K_L \mid K_S > - \\ ia^*b(\lambda_S^* - \lambda_L) < K_S \mid K_L > \tag{2.27}$$

Equating eq. (2.25) and (2.27) and noting that

$$\gamma_{S,L} = \sum_{k=1}^{n} |< k \mid T \mid K_{S,L} >|^2 \tag{2.28}$$

gives the relationship

$$(\lambda_L^* - \lambda_S) < K_L \mid K_S >= i \sum_{k=1}^{n} < k \mid T \mid K_L >^* < k \mid T \mid K_S > \tag{2.29}$$

This is the unitarity condition for the neutral kaons and is generally referred to as the Bell-Steinberger relation [40]. The relation can also be written as

$$< K_S \mid K_L >= \frac{\sum_{k=1}^{n} < k \mid T \mid K_S >^* < k \mid T \mid K_L >}{\frac{\gamma_S + \gamma_L}{2} + i\Delta m} \tag{2.30}$$

which is equivalent to

$$< K_S \mid K_L >= \frac{\sum_{k=1}^{n} (\gamma_k)_S \eta_k}{\frac{\gamma_S + \gamma_L}{2} + i\Delta m} \tag{2.31}$$

where η_k is defined as $\frac{<k|T|K_L>}{<k|T|K_S>}$ and $(\gamma_k)_S$ is the partial width of K_S to the various decay channels k. In terms of the T and CPT violation parameters eq. (2.31) can be written as

$$< K_S \mid K_L >= 2(Re(\epsilon_T) - iIm(\delta_{CPT})) \tag{2.32}$$

If one assumes that $\eta_{\pi^0\pi^0} = \eta_{\pi^+\pi^-}$ [29, 41], only takes into account $\pi\pi$ decay modes which are dominating and neglects[2] ϵ' it is possible to relate

[2]Assuming CPT symmetry in the decay matrix and decomposing the parameter ϵ' into the strong isospin states I=0 and I=2, ϵ' can be written in terms of the weak amplitudes A_0 and A_2 and the final state $\pi\pi$ strong interaction phase shift $\delta_2 - \delta_0$ [29, 42]:

$$\epsilon' = Im(\frac{A_2}{A_0} e^{(\delta_2 - \delta_0 + \pi/2)})$$

The ϵ' is suppressed by the $\Delta I = 1/2$ rule. The $\pi\pi$ scattering phase shift has been measured in pion nucleon scattering to be $(\delta_2 - \delta_0) = -(43 \pm 5)^\circ$, and $\varphi_{\epsilon'} = (47 \pm 5)^\circ$. Since ϵ' is small and the phase anyway happens to coincide with the phase of $\eta_{\pi^+\pi^-}$ it may be neglected in eq. (2.33) .

eq. (2.31) to the measurable quantity $\eta_{\pi^+\pi^-}$ according to

$$\eta_{\pi^+\pi^-} = < K_S \mid K_L > (i\frac{\Delta m}{\gamma_S} + \frac{1}{2}) \tag{2.33}$$

In eq. (2.33) also γ_L is neglected since it is small compared to γ_S. According to eq. (2.32) the quantity $< K_S \mid K_L >$ is real in case of CPT symmetry (T-violation) and imaginary for T symmetry (CPT-violation). This introduces a phase difference of 90° between the two cases. The present experimental value for $\varphi_{\pi^+\pi^-}$ [29] is

$$\varphi_{\pi^+\pi^-} = (44.3 \pm 0.8)° \tag{2.34}$$

This can be compared to the phase of the right hand side of eq. (2.33) assuming CPT invariance [29]:

$$\varphi_T = tan^{-1}[\frac{2(m_L - m_S)}{\gamma_S}] = (43.59 \pm 0.15)° \tag{2.35}$$

In case of T invariance the expected phase becomes

$$\varphi_{CPT} = \varphi_T + 90° \tag{2.36}$$

This indicates that CPT is mainly conserved in the mixing matrix **M** since the value for $\varphi_{\pi^+\pi^-}$ is much closer to φ_T than it is to φ_{CPT}. Note, however, that it is not possible to estimate $Re(\delta_{CPT})$ through the unitarity relation.

In the scheme above the comparison of the phases should rather be regarded as an indirect test of the consistency of a CPT invariant phenomenology than a measurement of T and CPT violation parameters. This indirect test through measurements of $\eta_{\pi^+\pi^-}$, Δm and γ_S has been performed very accurately by several groups [43, 44] and also by CPLEAR [45, 46, 47].

2.6 Measured semileptonic asymmetries in CP-LEAR

By studying the semileptonic decays of the neutral kaons one can keep track of the K^0 versus $\overline{K^0}$ content of the K_L and K_S physical states. This

provides the opportunity to measure directly the CPT and T violating parameters [48, 49] as defined in eq. (2.16) and (2.17). The semileptonic decays can also be used to measure the K_L–K_S mass difference (Δm) and the parameter x which describes a possible violation of the $\Delta S = \Delta Q$ rule. The definition of x is:

$$x = \frac{< \pi^- l^+ \nu_l | T | \overline{K^0} >}{< \pi^- l^+ \nu_l | T | K^0 >} \tag{2.37}$$

According to the $\Delta S = \Delta Q$ rule in the quark model, the decays $K^0 \to \pi^- l^+ \nu$ and $\overline{K^0} \to \pi^+ l^- \overline{\nu}$ are allowed while the decays $K^0 \to \pi^+ l^- \overline{\nu}$ and $\overline{K^0} \to \pi^- l^+ \nu$ are forbidden.

There are four different rates of semileptonic decays of neutral kaons that we label according to the neutral kaon produced in the annihilation and the observed decay as is shown in Table 2.1. Assuming $\Delta S = \Delta Q$ the last two rates require an oscillation of $\overline{K^0}$ to K^0 or inverse.

Rate	Produced kaon	Observed decay
R^+	K^0	$\pi^- l^+ \nu$
$\overline{R^-}$	$\overline{K^0}$	$\pi^+ l^- \overline{\nu}$
R^-	K^0	$\pi^+ l^- \overline{\nu}$
$\overline{R^+}$	$\overline{K^0}$	$\pi^- l^+ \nu$

Table 2.1: *Definition of the semileptonic rates*

Expressions for the semileptonic decay rates of neutral kaons in (2.1) can be deduced by solving the time dependent Schrödinger equation using the expressions in (2.18)-(2.19) for $\mid K_S >$ and $\mid K_L >$ and keeping only terms to the first order in the small parameters x, ϵ_L and ϵ_S:

$$\begin{aligned} R^+ \;\propto\; & [1 + 2Re(x) + 2Re(\epsilon_S) - 2Re(\epsilon_L)]e^{-\gamma_S t} \\ + \; & [1 - 2Re(x) - 2Re(\epsilon_S) + 2Re(\epsilon_L)]e^{-\gamma_L t} \\ + \; & 2e^{-\gamma t}\cos(\Delta m t) \\ + \; & 4[-Im(x) - Im(\epsilon_S) + Im(\epsilon_L)]e^{-\gamma t}\sin(\Delta m t) \end{aligned}$$

$$\overline{R^-} \;\propto\; [1 + 2Re(x) - 2Re(\epsilon_S) + 2Re(\epsilon_L)]e^{-\gamma_S t}$$

$$
\begin{aligned}
&+ [1 - 2Re(x) + 2Re(\epsilon_S) - 2Re(\epsilon_L)]e^{-\gamma_L t} \\
&+ 2e^{-\gamma t}\cos(\Delta m t) \\
&+ 4[Im(x) + Im(\epsilon_S) - Im(\epsilon_L)]e^{-\gamma t}\sin(\Delta m t)
\end{aligned}
$$

$$
\begin{aligned}
R^- \propto\ & [1 + 2Re(x) - 2Rc(c_S) \quad 2Re(\epsilon_L)]e^{-\gamma_S t} \\
&+ [1 - 2Re(x) - 2Re(\epsilon_S) - 2Re(\epsilon_L)]e^{-\gamma_L t} \\
&+ 2[-1 + 2Re(\epsilon_S) + 2Re(\epsilon_L)]e^{-\gamma t}\cos(\Delta m t) \\
&+ 4[-Im(x)]e^{-\gamma t}\sin(\Delta m t)
\end{aligned}
$$

$$
\begin{aligned}
\overline{R}^+ \propto\ & [1 + 2Re(x) + 2Re(\epsilon_S) + 2Re(\epsilon_L)]e^{-\gamma_S t} \\
&+ [1 - 2Re(x) + 2Re(\epsilon_S) + 2Re(\epsilon_L)]e^{-\gamma_L t} \\
&+ 2[-1 - 2Re(\epsilon_S) - 2Re(\epsilon_L)]e^{-\gamma t}\cos(\Delta m t) \\
&+ 4[Im(x)]e^{-\gamma t}\sin(\Delta m t)
\end{aligned} \tag{2.38}
$$

The decay widths of K_S and K_L are denoted γ_S and γ_L respectively, and $\gamma = (\gamma_S + \gamma_L)/2$. We define the following asymmetries which are sensitive to the parameters we want to determine:

$$A_T = \frac{\overline{R}^+ - R^-}{\overline{R}^+ + R^-} \tag{2.39}$$

$$A_{CPT} = \frac{\overline{R}^- - R^+}{\overline{R}^- + R^+} \tag{2.40}$$

$$\delta = \frac{R^+ + \overline{R^+} - (R^- + \overline{R^-})}{R^+ + \overline{R^+} + (R^- + \overline{R^-})} \tag{2.41}$$

$$A_1 = \frac{R^+ + \overline{R}^- - (\overline{R}^+ + R^-)}{R^+ + \overline{R}^- + \overline{R}^+ + R^-} \tag{2.42}$$

In the fits to determine the desired parameters (see Chapter 7) the theoretical rates as defined in eq. (2.38) are fitted to the measured asymmetries.

Using the theoretical expressions eq. (2.38) in the asymmetries eq. (2.39)-(2.42) we obtain the following:

$$A_T = 4Re(\epsilon_T) \tag{2.43}$$

$$\begin{aligned} A_{CPT} &= \frac{D_1}{D_2} \quad (\simeq 4Re(\delta_{CPT});\ \ t >> \tau_S) \\ D_1 &= 4Re(\delta_{CPT})(e^{-\gamma_L t} - e^{-\gamma_S t}) \\ &- 2Im(\delta_{CPT})sin(\Delta m t)e^{-\gamma t} \\ D_2 &= e^{-\gamma_L t} + e^{-\gamma_S t} + 2cos(\Delta m t)e^{-\gamma t} \end{aligned} \tag{2.44}$$

$$\begin{aligned} \delta &= \frac{2E_1}{E_2} \quad (\simeq 2Re(\epsilon_L);\ \ t >> \tau_S) \\ E_1 &= Re(\epsilon_S)e^{-\gamma_S t} + Re(\epsilon_L)e^{-\gamma_S t} - \\ &\quad [Re(\epsilon_S + \epsilon_L)cos(\Delta m t) + \\ &\quad 2Im(\delta_{CPT})sin(\Delta m t)]e^{-\gamma t} \\ E_2 &= e^{-\gamma_S t} + e^{-\gamma_L t} \end{aligned} \tag{2.45}$$

$$A_1 = \frac{2\cos(\Delta m t)e^{-\gamma t}}{(1 + 2Re(x))e^{-\gamma_S t} + (1 - 2Re(x))e^{-\gamma_L t}} \tag{2.46}$$

A non zero value for the A_T asymmetry provides direct evidence of T-violation, as was first pointed out in Ref. [50]. Assuming $\Delta S = \Delta Q$ the A_T asymmetry is a measure of the difference in the transition rates $\overline{K^0} \rightarrow K^0$ and $K^0 \rightarrow \overline{K^0}$. These processes are each others time inverse. As can be seen in 2.43 this asymmetry is constant as a function of time. Similarly, a deviation from zero in the asymmetry A_{CPT} is a signal for CPT-violation. This asymmetry is not independent of lifetime, but for times longer than around three τ_S, this expression is equivalent to $4Re(\delta_{CPT})$. The semileptonic charge asymmetry δ is, for lifetimes longer than around three τ_S, equal to $2Re(\epsilon_L)$. Since this charge asymmetry has been accurately measured for K_L [29] it is used to determine the detection efficiency $\eta = \frac{\epsilon(\pi^+ l^-)}{\epsilon(\pi^- l^+)}$ which is a few percent above one. In eq. (2.39), eq. (2.40) and eq. (2.45) the parameter x is assumed to be zero. The upper limit of this parameter is of the order 0.01 [51, 52] and small enough to make it negligible in these expressions. The quantities Δm and $Re(x)$ can be determined by fitting asymmetry A_1 where Δm determines the frequency and $Re(x)$ the amplitude of the oscillation.

Chapter 3

Experimental set-up

3.1 Demands on the detector

The CPLEAR detector [53], which is displayed in Fig. 3.1 and 3.2, mainly needs to fulfill the following requirements:

a. The branching ratio of the golden channel $p\bar{p} \rightarrow K^{\pm}\pi^{\mp}\overline{K^0}(K^0)$ is only 4/1000 compared to the rest of the annihilation channels and a very large number of golden events needs to be collected in order to measure the physics parameters with the desired small statistical errors. So both high acceptance for the signal and high rejection of the backgrounds should be combined. In general, the detector must cope with a high initial rate ($1\ MHz$) that must be reduced to a level acceptable for writing to tape ($0.5\ kHz$).

b. For the T violation parameter $Re(\varepsilon_T)$ eq. (2.39) around 10^6 events are required for a statistical error of the order $0.5 \cdot 10^{-3}$. The large number of events needed implies datataking for several years. This means the detector should not be sensitive to aging and it must be radiation hard enough to withstand the accumulated dose.

c. The regeneration effect [54] means that K^0 and $\overline{K^0}$ are transformed into each other through interactions in the detector. Since the am-

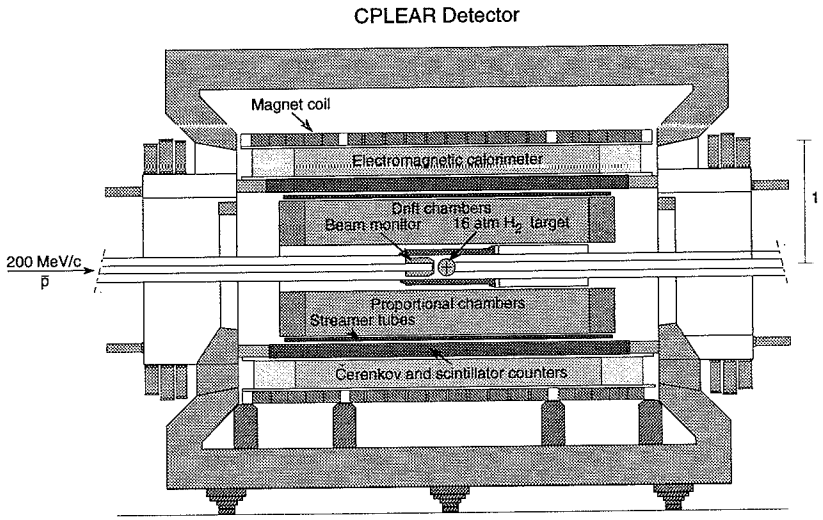

Figure 3.1: *Longitudinal view of the CPLEAR detector. The antiprotons from LEAR annihilate in the target indicated as a sphere in the center of the detector. The target is surrounded by proportional chambers, drift chambers, streamer tubes, particle identification detector, calorimeter and magnet. The coordinate system used in the analysis is defined with its origin in the center of the detector and the z axis coincides with the symmetry axis of the detector. The side of the detector facing the incoming $\overline{p}$ is referred to as upstream and the other side as downstream*

plitude and phase of the regeneration is not very well known, this is difficult to correct for and will, if not kept to a low level, significantly contribute to the systematic errors. For this reason a minimum of material should be used in the detector volume.

d. Since several of the quantities to be measured are time dependent the tracking system must give a resolution in the calculated decay time of around 0.5 τ_s[1]. It is also important to achieve good resolution in the tracking system to reject background with kinematic and geometrical cuts.

e. The detector volume should be large enough to contain a substantial fraction of the K_L decays but, on the other hand, it has to fit

[1] $\tau_s = 0.892 \cdot 10^{-10}$s; lifetime of K_S

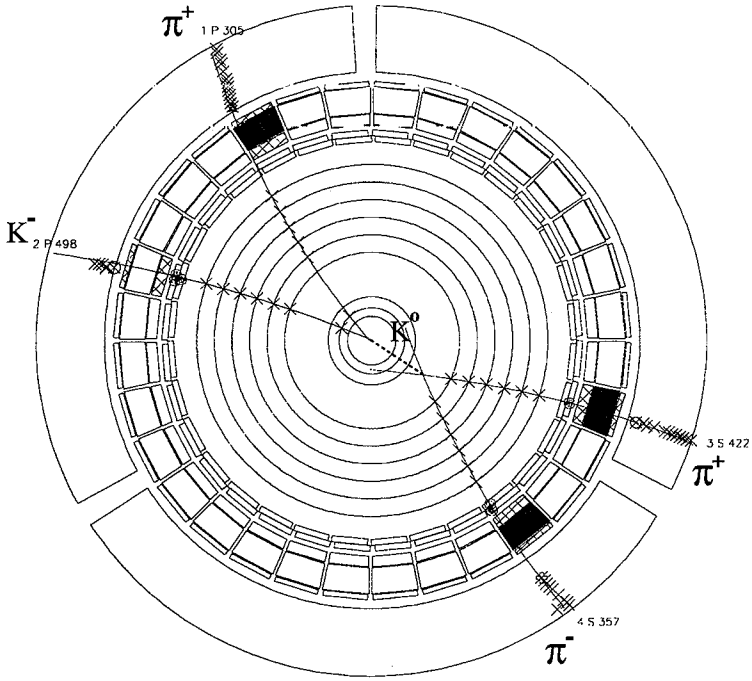

Figure 3.2: *Transverse view of the CPLEAR detector*

in the existing DM2 magnet [55]. This was achieved by making the calorimeter [56] thinner than would otherwise have been the case. Around 1/15 of the K_L particles decay inside of the detector. The time dependence of the measured asymmetries is at lifetimes shorter than 20 τ_S. This corresponds approximately to 60 cm, which matches the outer radius of the tracking system.

3.2 Antiprotons, Target and Magnet

The antiprotons are delivered from the storage ring for Low Energy Antiprotons (LEAR) at CERN with a momentum of 200 MeV/c at a rate of 1 MHz. There is a dedicated beam line to the CPLEAR detector. A

beam counter [57] detects the antiprotons and issues either a start signal to the trigger or a veto if two antiprotons arrive within 120 ns. Two proportional chambers orthogonal to each other serve as a beam monitor. If the beam is out of focus this is quickly detected and it is automatically refocused [58].

The beam passes through a beryllium degrader that reduces the $\overline{p}$ energy so that they stop in the middle of the target. The target is a kevlar sphere of radius 7 *cm* filled with hydrogen gas at a pressure of 15 atm. The antiprotons enter the target through a mylar window with a diameter of 11 *mm*. Because of the straggling, the stopping distribution of the antiprotons will be approximately Gaussian shaped with a FWHM of 5.9 *cm* along the beam axis. In the transverse plane the distribution has FWHM of 1.1 *cm*. When the antiprotons stop they will form an antiproton-proton atom before annihilating. The annihilation process itself is still subject to research [59] since the strong interaction cannot be treated perturbatively at low energies.

The magnetic field is uniformly 0.44 T and the field lines are parallel to the longitudinal symmetry axis of the detector. To cancel geometrical asymmetries of the detector the magnetic field is normally reversed three times every 24 hours of data taking. The normal magnetic field (when the field lines are parallel to the z-axis) is referred to as M1 while the reversed field (when the field lines are anti parallel to the z-axis) is referred to as M2. Half of the data is recorded with M1 and the other half with M2.

3.3 The tracking system

3.3.1 Multi Wire Proportional Chambers

Two multi wire proportional chambers [60] denoted PC1 and PC2 are situated at radii of 9.5 *cm* and 12.7 *cm* (see Fig. 3.2). PC1 and PC2 both have an efficiency of 97% giving a combined efficiency of 99.9%. The definition of a primary track for the trigger is a track with at least one PC hit since such a track might be associated with the primary vertex. A hit map for each event is sent to the trigger. The hitmap is used to determine the total number of tracks and the number of primary tracks.

The gas mixture is 79.5% argon, 20 % isobutane and 0.5% freon as quencher. The chamber walls are constructed from kapton/rohacell and are separated by 10 *cm*. The spacing between the wires is 1.039 *mm*. The wires are made of goldplated tungsten. The resolution of the chambers is 340 μm in the transverse plane.

3.3.2 Drift chambers

The six drift chambers [61] have radii between 25.5 *cm* and 50.9 *cm*. The gas mixture is 50% ethane and 50% argon. The active volume of each chamber is 10 *cm* thick and the walls are made of mylar. For the drift chambers, as for PC1 and PC2, goldplated tungsten wires are used as sense wires. The sense wires are grouped in doublets with a distance between the wires of 0.5 *mm* to avoid left/right ambiguities in the trigger. The wires are kept at a voltage of 2200 V. Field shaping wires are put between the sense wires at intervals of 10 *mm*. Cathode strips of gold 5.5 *mm* wide and 50 nm thick are deposited on the mylar and are read out for drift chambers 1, 2, 4 and 6.

The efficiency of the drift chambers is 97% for the wires and 95% for the strips. The hitmap from the drift chambers is sent to the trigger in order to check the number of tracks and also to cut low energy $\pi^{\pm}$ faking $K^{\pm}$ at an early stage. Later in the trigger the drift times are used to parameterize the tracks.

The resolution of the drift chambers is 300 μm in the transverse plane and 2 *mm* in the z direction. This results in a transverse momentum resolution $\frac{\Delta p}{p}$ of 5% at 300 MeV/c.

3.3.3 The streamer tubes

The two layers of streamer tubes [62] have radii of 58.2 *cm* and 60.0 *cm* respectively and are the outermost tracking devices. The function of the streamer tubes is to provide the trigger with a fast z-coordinate for the on-line track parameterization. Assuming that the track originates from the center of the detector, the streamer tube information gives an estimate of the momentum component in the z-direction. The efficiency

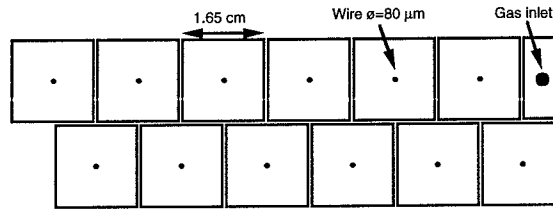

Figure 3.3: *Cross section of one (of 32) group of 12 streamer tubes. The wires and the gas inlet are indicated in the figure. Note that the streamertubes will be asymmetric to tracks of opposite curvatures because of the displacement of the inner and outer layer.*

of the streamer tubes is 92% per layer.

The streamer tubes consist of 32 sectors with 0.5 *mm* thick walls made of an aluminum/magnesium alloy and each having the dimensions of 16.5 *mm* x 16.5 *mm* x 2520 *mm*. The two layers in one sector are slightly offset (see Fig. 3.3) to prevent particles from escaping between two sectors. Unfortunately this introduces an asymmetry in the detection efficiency for tracks of different curvature. The streamer tubes operate at a voltage of 4000 V and have a gas mixture of 50% argon, 46% isobutane, 4% methylal and 0.008% freon. Groups of three tubes are multiplexed to a three channel TDC and one can get the z-coordinate from the upstream downstream time difference through a fast hard ware look up table. The online resolution of the streamer tubes is 1.4 *cm*.

3.4 Particle Identification Detector (PID)

The particle identification detector Fig. 3.4 and 3.5 constitutes together with the proportional chambers and drift chambers, the heart of the CPLEAR detector. All CP violation experiments need good particle identification but in CPLEAR this is particularly important since a 4 permille kaon signal must be separated from all other annihilation channels.

Each of the 32 PID modules (see Fig. 3.4) is constructed with a

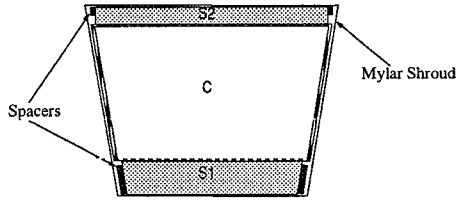

Figure 3.4: *Section of the PID detector, transverse view.*

Cherenkov detector sandwiched between two scintillators. The idea is to use the scintillators as hodoscopes and the Cherenkov as a threshold device for the first trigger stage. The Cherenkov gives a signal for the π but not for the K since the refractive index of the Cherenkov medium has been chosen in such a way that most of the $\pi^{\pm}$ (which are faster due to the lower mass) emit Cherenkov light while the slower $K^{\pm}$ do not.

The signals from the scintillators and the Cherenkov are also digitized and used at later trigger stages for more refined cuts on the particle hypothesis using both the ionization loss dE/dx and time of flight (TOF). These values are also used offline for further selection of, in my case, semileptonic decays of neutral kaons. The position of the PID (inner radius 62 *cm* and outer 76 *cm*) between the streamer tubes and the calorimeter is indicated in Fig. 3.1 and Fig. 3.2. In Fig. 3.4 is shown a cross section of the PID. Each of the 32 PID sectors have a trapezoidal form (Fig. 3.4) such that they form a cylindrical shell when put together.

To have the PM-tubes outside the magnetic field, lightguides around 1 *m* long are glued to the ends of the scintillators and the Cherenkov counters. The lightguides pass through rectangular holes in the endcap of the magnet where four PM-tubes are situated in each end of the PID sectors (Fig. 3.5). Unfortunately, this arrangement requires the PM-tubes to be dismounted whenever one needs to remove the endcaps, e.g. to work on the drift chambers.

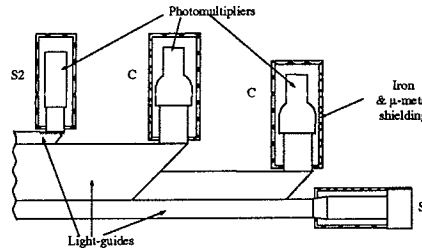

Figure 3.5: *Mounting of the PM-tubes of the PID*

3.4.1 Scintillators

The first scintillator (S1) is 3 *cm* thick and is used both for a dE/dx measurement and for a TOF measurement. The main task of the second scintillator (S2) is to check that the particle actually traversed the Cherenkov. Since it is not used for TOF measurements, for which a high light output is essential, it is only 1.4 *cm* thick. Both scintillators are made of plastic material. Plastic is a good material since it is easy to handle, the light output is good and a fast signal is offered. The decay constant is only of the order of 2 *ns*. The materials are BC408 from Bicron for S1 and NE102 from Nuclear Enterprises for S2. At the end of the lightguides there are PM-tubes of type XP4222B for S1 and XP2232B for S2. The XP4222B fulfills the demands of good timing, which is needed for the S1, and the obtained resolution is 180 *ps*.

3.4.2 Cherenkov counters

Each of the 32 Cherenkov counters is 8 *cm* thick and the width is 12 *cm* and 13.6 *cm* at the inner and outer radii. The modules were fabricated in Gothenburg from extruded PMMA and the walls are 2.5 *mm* thick. Each module has a volume of 32 liters. The index of refraction for the C_6F_{14} liquid ($n = 1.26$) results in a Cherenkov threshold close to the desired $\beta = 0.81$ corresponding to the maximum $K^{\pm}$ velocity. The properties of the liquid are described in detail in chapter 4. The PM-tube used for the Cherenkov detector is Philips XP3462 and, to increase the efficiency,

two of them are put at each end of the counter and the lightguide is split to direct light into both. For the Cherenkov counters the detection efficiency is more important than for the scintillators and also the emitted wavelength is shorter. These PM tubes have good quantum efficiency in this wavelength interval. For 300 MeV/c $\pi^{\pm}$ incident at z=60 cm the number of photo-electrons per PM is 9.6 . The number of photo-electrons increases for larger z when the particle traverses the Cherenkov module closer to the PM tubes at one end.

3.4.3 Readout of the PID

The signals from the Cherenkov counters are amplified a factor 10 while the scintillator signals do not need to be preamplified. The signal is split into several branches, one for the first level trigger and another for higher trigger levels. The S1 signal is also split into a TDC branch.

The signal for the first level trigger is passed to discriminators and further to the decision logic looking for $S\bar{C}S$ [2]. Within 115 ns the multiplicity and the number of $K^{\pm}$ candidates are determined.

The S1 signals for the TDC branch are first passed through constant fraction discriminators before they are converted in 1.2 μs by a flash TDC [63] of 10 bits accuracy having a full scale of 70 ns. For the later trigger levels, the S1 and Cherenkov signals are passed to flash ADC's [64]. The conversion takes 400 ns and the converted value is stored in a buffer to be read by HWP2 (see section 3.6), and if the event is accepted, read out.

3.5 Calorimeter

The high granularity electromagnetic calorimeter is not used in the analysis presented in this thesis. A detailed description can be found in [56], and results for the $K^0(\overline{K^0}) \rightarrow \pi^0\pi^0$ decay channel is given in [65].

[2] $S\bar{C}S$ is a track giving a signal in both scintillators but no signal in the Cherenkov

3.6 The Trigger

Since it is not possible to write 1 MHz of events to tape considering that the size of a typical event is 2.5 kbytes, the trigger has to discard online non-golden events to decrease the data flow to around 0.5 kHz, i.e. a factor 2000 [66]. The different trigger stages are described in the following sections. Only for calibration purposes the trigger is sometimes bypassed and, in that case, only at least one S1 hit is demanded for an event.

3.6.1 Early Decision Logic (EDL)

In the EDL, events are selected according to the number of $K^{\pm}$ signatures and the S1 hit map. To optimize the number of golden events written to tape the number of $K^{\pm}$ signatures is, in the standard trigger, demanded to be greater than or equal to one while the number of S1 hits is demanded to be greater than or equal to two. The decision time is 60 ns and the reduction of the rate is a factor 4.1.

3.6.2 The p_T cut

Since $\pi^{\pm}$ with a momentum below around 270 MeV/c will have a velocity below the threshold of the Cherenkov counters, they will fake $K^{\pm}$ [67]. The p_T cut reduces the number of these events. This is done by comparing the number of the wire hit in DC1 with that of the wire hit in DC6 for the $K^{\pm}$ candidate (Fig. 3.6) compared to a track with no curvature. A difference in wires of 1 corresponds to a transverse momentum of 800 MeV/c, a difference of 2 to 400 MeV/c, a difference of 3 to 270 MeV/c while a 4 wire difference indicates a transverse momentum of 200 MeV/c. The correlation between the number of wire hits and the momentum is based on the assumption that the tracks originate from the center of the detector and that the DC1 and DC6 are perfectly concentric with the symmetry axis of the detector. In the standard trigger, events must have at least one $K^{\pm}$ candidate with a transverse momentum of more than 270 MeV/c. The decision time is 400 ns and the rate reduction is a factor 3.1. Since DC1 is not perfectly aligned relative to DC6 the p_T cut (Fig. 3.6)

introduces a difference between K^+ and K^- depending on whether the magnetic field is reversed or not. This effect will cancel out if one mixes equal amounts of M1 and M2 data.

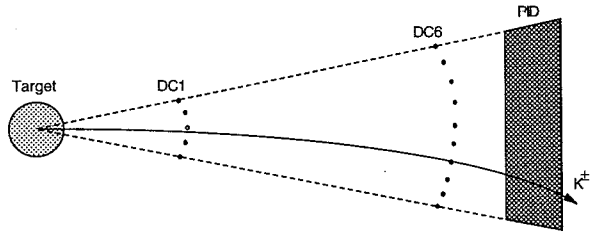

Figure 3.6: *The p_T cut is made on kaon candidates by comparing the number of the wire hit in DC1 to the number of the wire hit in DC6 compared to a straight line (not drawn to scale).*

3.6.3 On line cuts on the number of tracks

A set of different combinations of the number of tracks and the number of primaries is allowed. The combinations that are normally requested are that the number of tracks has to be 2, 3 or 4 and the number of primaries has to be 2 in the first case, 2 or 3 in the second case, and between 2 and 4 in the third case. The cuts on the number of tracks are made at different stages of track parameterization as described in the following three paragraphs. After those three steps cuts are only made on the features of the primary tracks and the secondary tracks are not involved.

Intermediate Decision Logic (IDL)

The hit maps for PC1 OR PC2, DC1 OR DC2 and DC5 OR DC6 are compared for different sectors of the PID. From this comparison the total

number of tracks, as well as the number of primary tracks, are deduced. A primary track is defined as a track with at least one PC hit. The decision time is 80 ns and the reduction factor for the rate is 1.9 .

Track Follower

The tracks as defined in the IDL are now traced from their S1 hit by the track follower. The track follower starts from the S1 and the outermost drift chamber DC6. It then works inwards in such a way that it looks for a hit to connect to the track in the next inner layer of the tracking system in the neighborhood of where the last hit was found If no hit is found the track is denoted as bad and if no hits are found for two consecutive layers the track is considered as lost. The total charge of all tracks is also demanded to be zero at this stage.

Simple fit of the tracks

A simple fit is made of each primary track identified by the track follower and the number of tracks for which the fit converges is again counted. The number of $K^{\pm}$ candidates at this stage has to be less than or equal to two. Every track is parameterized with three parameters and the result from the fit is stored for further use in the trigger.

3.6.4 Kinematics

The missing mass and the sum of the momenta for the primary $\pi^{\pm}$ and $K^{\mp}$ are computed. Since the latter is faster to calculate, and, in fact, has much the same effect as a cut on the missing mass, the sum of the momenta is used in the trigger for the data analyzed in this thesis. This sum is demanded to be above 760 MeV/c. The decision time on the information compiled from the track follower and the fit and the kinematics is 3.6 μs and the reduction of the rate is 2.7 .

3.6.5 Hardware Processor 2 (HWP2)

HWP2 makes cuts on dE/dx, the amount of Cherenkov light and TOF, as measured by the PID, in combination with the kinematic variables for

each track. The expected energy loss is compared to the measured dE/dx and, if the difference is more than two standard deviations for all possible combinations of primaries, the event is rejected. Also, the TOF difference between the primaries is compared to what is expected for a $K^{\pm}\pi^{\mp}$ and the number of photoelectrons for the primary tracks must agree with the $K^{\pm}\pi^{\mp}$ within two standard deviations. For HWP2 the decision time is 1.9 μs, while the reduction of the rate is 6.4 .

3.6.6 Hardware Processor 2.5 (HWP2.5)

This processor counts the number of showers in the calorimeter but is only active for events with only two charged tracks and therefore is not used for the data in this thesis.

3.7 Data acquisition

The data acquisition system is based on a VME bus controlled by a a Valet system [68] and there is a dedicated Valet (Root Readout in Fig. 3.7) for each subdetector. When an event passes all trigger stages, a signal is issued to transfer the data from the front end electronics to the Valets. The Events Builder puts the information from the different subdetectors together into a whole event and passes the event further through an Optical link to a Data Distribution System that in turn sends all events to two IBM tapedrives. To continuously monitor the detector performance some events are also sent to a monitoring system that includes, for example, an event display. Vax computers are used for the general control of the DAQ. A diagram of the data acquisition system is given in Fig. 3.7.

3.7.1 Possible improvements of the trigger

The total deadtime of the data acquisition is around 50%. This is mainly due to the transfer time from the root readout to the event builder. If this could be speeded up it would significantly increase the number of good events written to tape. Other ways of decreasing the dead time are to reduce the rate of events even more than has been described above or to make the trigger decisions faster.

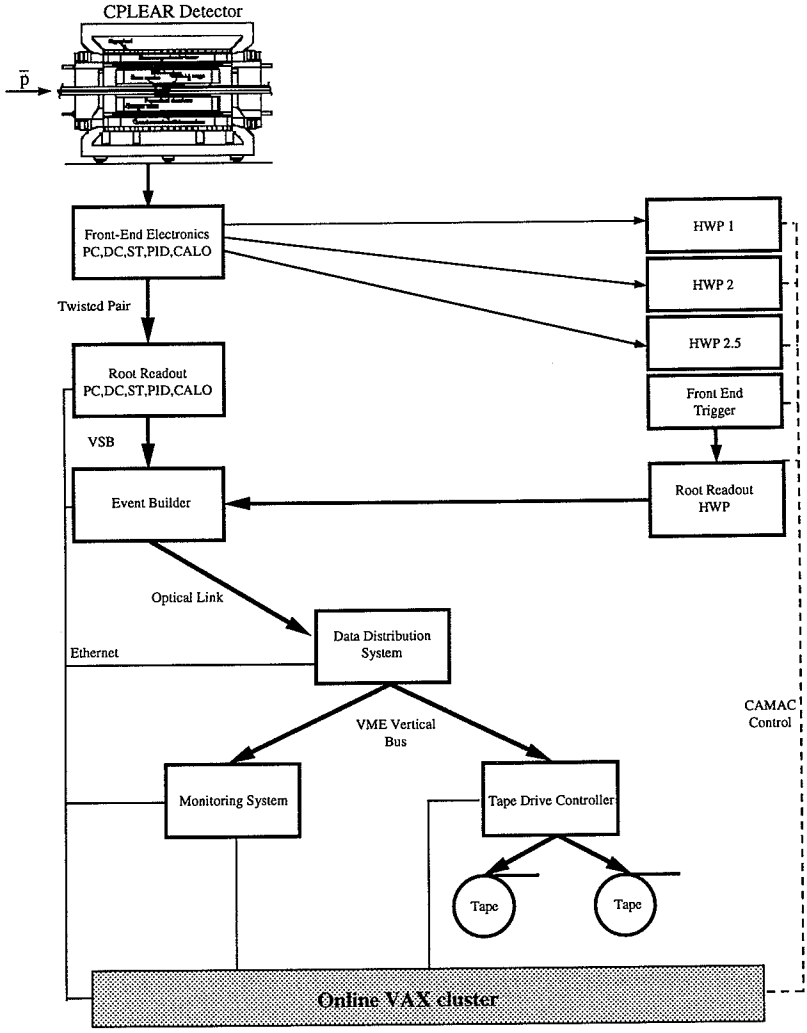

Figure 3.7: *Overview of data acquisition system. The paths of the information from the detector are shown together with the interaction between the trigger and the data acquisition system.*

In 1995 an extra proportional chamber was fitted into the detector [69] by making the target smaller. The demand of only two detected tracks in this chamber already at the EDL level enables an additional rate reduction of a factor 4 and increases the number of good events to tape by almost 40%.

During the course of the experiment various other methods of reducing the trigger rate have been proposed but not implemented in the actual trigger used for data taking. In Ref. [70] a way of replacing the track follower with a neural network to recognize the patterns of good events is described. In addition, an idea of this author describing how to increase the speed of the trigger decisions is presented in [71]. Here the gain would come from a cut based on the S1 dE/dx after 500 ns rather than the current 6 μs with the HWP2. An estimation of the momentum at this early stage can be obtained from the p_T cut together with a z-coordinate from the difference in amplitude in the S1. This would, according to simulations, result in an increased number of good events to tape of around 15%. There is, however, a danger in interfering with a working system and therefore these suggested improvements have not been implemented.

Chapter 4

Ultrasonic treatment of the C_6F_{14} liquid Cherenkov radiator

4.1 Cherenkov liquid

Cherenkov counters are frequently used in physics experiments to identify particles traveling at different speeds. A particle that traverses the radiator material with a velocity v exceeding the velocity of light in the medium ($v > \frac{c}{n}$; c=velocity of light in vacuum, n=index of refraction), emits Cherenkov light, which is detected. In a given application the index of refraction has to be chosen to match the velocities of the particles. To collect a sufficient number of photons in the sensitive spectral range of the photon to electron converter, the radiator material should also be transparent in the UV, possibly down to below 170 nm. Useful radiator materials with low indices of refraction n are very rare [72, 73, 74]. C_6F_{14} (FC-72 [1]) has n 1.28 to 1.26 in the range of 150 nm to 300 nm and is extensively used in high energy physics [75, 76, 77].

Unfortunately, C_6F_{14} has a high solubility for air, 48 ml at atmospheric pressure and 20 ^oC per 100 ml of liquid [78]. The factory delivered

[1] Trademark of 3M

C_6F_{14} usually contains too much dissolved air to be an efficient Cherenkov radiator without prior treatment. The problems from the dissolved gases can be due to gas that is released from the liquid (e.g. because of a temperature increase) thus forming gas bubbles in the Cherenkov liquid container. This is the case for CPLEAR, where particles which pass the Cherenkov detector through a gas pocket will not emit Cherenkov light and the efficiency of the Cherenkov counters will thus be decreased. An additional difficulty in the CPLEAR case was that only one plastic tube (diameter $2mm$) connects each Cherenkov counter to the outside of the detector. In order to degas the liquid a circulation of liquid needs to be achieved through this tube (see section 4.5). A second problem with dissolved oxygen is that it absorbs the Cherenkov light. The improvements of transmission of the C_6F_{14} through ultrasonic treatment is described in section 4.7.

4.2 Degassing methods

There are several methods available to reduce the amount of dissolved gas in liquids like C_6F_{14}. Apart from ultrasonic treatment one can e.g. repeatedly freeze the C_6F_{14} with liquid nitrogen or treat it with a chemical filter. To freeze it is a rather cumbersome procedure, often not possible to perform when the liquid is inside a detector. The chemical filtering process has been used successfully in some cases [79], but has the drawback that it may catalyze all kinds of unwanted reactions. The products of these reactions often absorb, just as the oxygen does, very strongly the light below 200 nm wavelength. Degassing by boiling or vacuum pumping, we found, require the use of an efficient condenser plant, and the liquid needs to be kept boiling for almost one hour. Wavelength shifters and other dopants in the liquid might disappear and during vacuum pumping oil from the pump may pollute the liquid. All these methods are complicated and sometimes unreliable.

With ultrasonic degassing the temperature of the C_6F_{14} stays below the boiling point and no special precautions are needed to avoid loss of liquid due to evaporation. Ultrasonic crystals can be placed inside or glued on to almost any container. Since we found it a cheap and very reliable method to do degassing, this was our choice.

4.3 Ultrasonic treatment

The principle of the ultrasonic degassing process [80] is that bubbles (in this case C_6F_{14} gas) are formed by cavitation from the ultrasound. Any gas dissolved in the liquid will then diffuse into the bubbles which are rapidly rising to the surface. The diffusion is much enhanced by the fact that the form of the bubbles is constantly changing because of the ultrasound. This means that the liquid layer closest to the bubble will be exchanged very quickly. The ultrasound also merges small, already existing, gas bubbles in the liquid to larger bubbles with greater buoyancy which accelerates the ascension to the surface of this gas. To test the ultrasonic performance 2.7 dm^3 of C_6F_{14} was put in an expansion vessel with an ultrasound crystal glued to the bottom (of the type described in 4.3.1). The amount of air emitted from the liquid was measured together with the temperature as a function of time once the ultrasound was turned on and this is displayed in Fig. 4.1 . Both quantities are almost linear with temperature up to 55 $°C$. If the treatment continues beyond 50 min no more gas comes out. Since 1.05 dm^3 was released from the liquid this batch of C_6F_{14} was 80 % saturated when delivered from the factory. The conclusion is that it is possible to drive out all dissolved gases from C_6F_{14} without exceeding the boiling point (55 $°C$).

4.3.1 Expansion system

Since it was impossible to reach the individual Cherenkov modules the treatment of the Cherenkov liquid had to take place outside the detector in ultrasonic baths that also served as expansion vessels for the liquid to avoid overpressure.

The ultrasonic baths were constructed from plexi-glass cylinders with a volume of 11 dm^3 and the bottom made of a steel plate with the ultrasonic head glued on the bottom side. The joint between the plexi-glass and the steel was made by an O-ring pressed with four screws. A floating plexi-glass plate in every vessel kept the liquid from contact with air. A pipe was connected from this plate to a plastic bag which was used to measure the amount of air coming out of the liquid. All vessels were cleaned with C_6F_{14} using the ultrasound before they were put into contact with the liquid from the counters. The O-ring gasket was made of viton

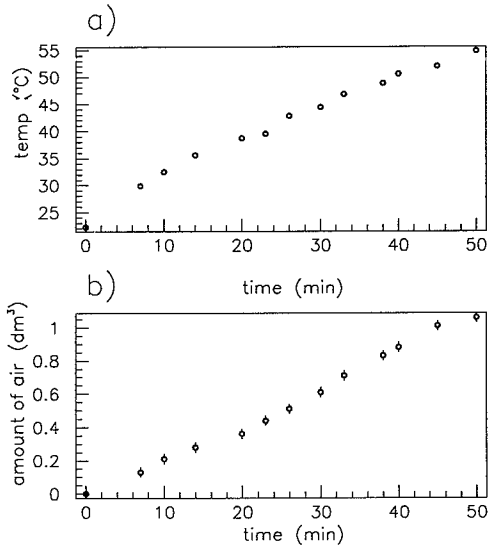

Figure 4.1: *Ultrasonic treatment of 2.7 dm^3 C_6F_{14}: In a) the temperature of the C_6F_{14} and in b) the amount of air coming out as a function of time during ultrasonic treatment is displayed. The test was done at normal atmospheric pressure and the ambient temperature was 25 °C .*

material. The 32 expansion vessels are kept in a rack where the relative height between the vessels is the same as the vertical distance between the Cherenkov counters in the detector in order to have all counters at the same pressure.

4.3.2 Transmission tests of the C_6F_{14}

All the materials used in the expansion vessels were tested in order to see that no pollutant from them decreased the transmission of the C_6F_{14}. These transmission tests[2] were performed from 190 *nm* to 250 *nm* by using

[2]The tests were made with a Perkin Elmer Lambda 15 spectrophotometer

two cells (diameter 5 *mm*) where one was filled with C_6F_{14} directly from the factory and used as a reference and compared to the other cell that contained the liquid to be tested. There was no change in transmission before and after the liquid had been in contact with any of the materials (for about a week) except for the plastic bags. The liquid which had been in contact with the plastic bag used to collect the air showed decreased transmission. We therefore carefully ensured that no liquid that had condensed in these bags went back into the expansion vessel.

4.4 Temperature of the Cherenkov counters

Since the solubility of air in C_6F_{14} decreases rapidly close to the boiling point the problems due to air bubbles in the Cherenkov modules is related to the temperature (see eq. (4.1)). In order to cool the entire detector several large fans were used. The temperature is monitored by two platinum precision probes mounted on every fourth PID module half a meter from the ends of the Cherenkov box in between the S2 and the Cherenkov. The temperature is strongly correlated to whether the calorimeter electronics is on or off and to the room temperature and it is also slightly dependent on the magnet temperature. When the degassing operation started the temperature for the hottest Cherenkov (the top Cherenkov counter) was 38 °C when the ambient temperature was 25 °C but when this temperature increased to around 40 °C the temperature of the liquid, was momentarily 45.5 °C. Since the temperature of the various counters inside the detector varies (counters around the top are hotter than the ones at the bottom of the detector) more degassing cycles are needed for some counters than for others.

4.5 The degassing

By increasing and decreasing the height of the rack (i.e. the overpressure in the Cherenkov counters) the size of the bubbles can be regulated and a circulation of liquid from the counters to the expansion vessels is achieved. The only hazard is that the overpressure might break the boxes containing the liquid. Since a test on a spare PID showed that it broke at an overpressure of 5 *bar* it was ad hoc assumed that the Cherenkov could

be exposed to an overpressure of around 1.5 *bar* without any significant risk of a leakage. The liquid that flows out of each module (around 8 dm^3 for the first degassing cycle) when it was not at any over pressure was degassed and subsequently fed back into the Cherenkov modules by increasing the over pressure to 1.7 *bar*. One degassing cycle lasted for 14 hours since this was the time required for the gas to dissolve. Once inside of the modules the degassed liquid absorbs part of the bubbles. Using Henry's law and the ideal gas law [81] it is possible to calculate the volume V_G of the gas bubble inside a Cherenkov counter for a certain pressure P:

$$V_G = V_{tot} \cdot 0.48 \cdot (\frac{T}{293}) \cdot \frac{(P_0 - P)}{P} \tag{4.1}$$

$$P = P_A + \rho g h - P_D \tag{4.2}$$

$$P_0 = \frac{n_0}{H(T) \cdot V_{tot}} \tag{4.3}$$

$$PV_G = (n_0 - n)RT \tag{4.4}$$

For $P \geq P_0$ the bubble size $V_G = 0$. V_{tot} is the total amount of liquid that is 32 l for each Cherenkov counter. The atmospheric pressure P_A was 961 *mbar* when the degassing started while the temperature T of the Cherenkov liquid was 311 K. The density ρ of C_6F_{14} is 1680 kg/m^3, g=9.82 m/s^2, h is the difference in height between the Cherenkov counters and the expansion vessels and P_D is the vapor pressure of the C_6F_{14} [3]. In eqn. 4.3 for P_0, $H(T)$ is a temperature dependent constant from Henrys law and n is the amount of dissolved gas in the liquid in *kmol* while n_0 is the total amount of gas in *kmol*. The value for P_0 was 690 *mbar* when the degassing started and subsequently decreased each degassing cycle when n_0 decreased. From these expressions one obtains an efficiency corresponding to a 1/6 reduction of the total air content (indicated by the parameter n_0) when 8 dm^3 of liquid (1/3 of the total amount in one Cherenkov module) is extracted, degassed and fed back in.

The problem of the bubbles was observed during a testrun over Easter 1992 when as a significant decrease in the pion rejection efficiency occurred simultaneously with a large amount of liquid being forced out from the counters into the expansion vessels by the growing bubbles. The degassing operation started when the ultrasonic expansion system was ready in the beginning of the major data taking in the summer 1992. Altogether eight degassing cycles were performed and the operation lasted for around one

[3] $P_D = 10^{7.6-1552/T} \cdot 1.33$ *mbar*[81]

week. Occasionally liquid had to be added into the expansion vessels since more and more liquid went into the counters when the bubbles were absorbed. This can be seen in Fig. 4.2, where the decrease of the bubble size, equivalent to the additional amount of liquid going into the counter after each degassing cycle, is displayed for a typical counter. During these eight degassing cycles the temperature of the Cherenkov liquid was around 43 °C. From the increase in pion rejection efficiency and from the plots according to Fig. 4.2 for each counter we deduce that more than 90% of the bubbles were gone. The remaining relatively small bubbles still left in a few of the counters were indicated by unstable liquid levels in their expansion vessels when the temperature changed. In a hitmap (Fig. 4.3) the fraction of tracks with golden signatures is indicated for each Cherenkov counter and is a measure of the inefficiency. The counters with remaining bubbles show a higher inefficiency than the rest. It can also be seen that counter 22, which was leaking already before the operation with the ultrasonic expansion system was started, has a particularly high inefficiency. The degassing procedure has been repeated before each data taking period to get rid of any air dissolved into the liquid between the runs.

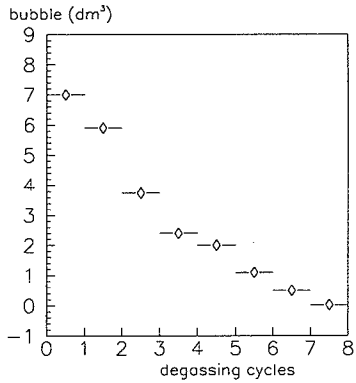

Figure 4.2: *Decrease of the bubble size in dm^3 for a typical Cherenkov counter during the eight degassing cycles. The initial bubble size has been assumed to be 7 dm^3 which is the bubble size observed in tests with a spare Cherenkov module at similar temperature.*

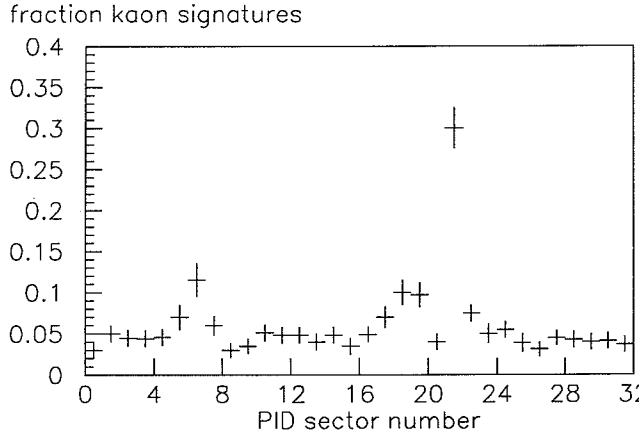

Figure 4.3: *Typical hitmap for the Cherenkov counters from a run at the end of 1992. Counter number 8 is at the top of the detector and the counters are numbered clockwise looking from the upstream side (Fig. 3.1). Apart from the leaking sector 22 and a few counters with small remaining bubbles the hitmap is flat.*

4.6 $\pi^{\pm}$ detection efficiency

To estimate the $\pi^{\pm}$ detection efficiency the annihilation channel $p\bar{p} \rightarrow \pi^{\pm}\pi^{\pm}\pi^{\mp}\pi^{\mp}$ is selected using a 4 constraint fit [82]. For the selected $\pi^{\pm}$ the inefficiency is taken as the fraction of events with a golden signature. This fraction is plotted as a function of momentum in Fig. 4.4 where the line indicates the average from 350 MeV/c to 700 MeV/c.

The performance of the PID has been continuously followed during the different run periods using the average of the fit in Fig. 4.4 . The variation of the $\pi^{\pm}$ detection inefficiency for the non leaking sectors from the data taking period P8 in the autumn 1990 to P26 in the autumn 1994 is displayed in Fig. 4.5 . In Fig. 4.5 the estimated efficiency without degassing is also indicated. In the P8 run the $\pi^{\pm}$ detection inefficiency

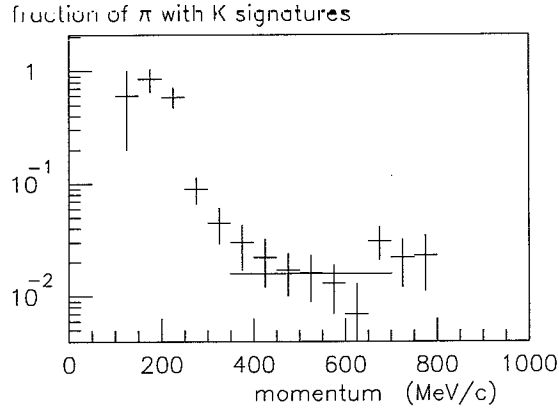

Figure 4.4: *Typical $\pi^{\pm}$ rejection inefficiency as a function of momentum. The increase for lower momenta is due to the Cherenkov threshold for $\pi^{\pm}$ at 270 MeV/c. The fit indicated in the figure is in the range 350 MeV/c to 700 MeV/c and the fraction of $\pi^{\pm}$ with a golden signature ($S\bar{C}S$) is* 0.016 ± 0.003 *with* $\chi^2 = 6.3/6$ *d.o.f. The fitted horizontal line is taken as a measure of the inefficiency displayed in Fig. 4.5.*

was around 10 permille [82] while in P13 the inefficiency increased due to several leaking counters [83] which were repaired before P17. In run P17-P26 the $\pi^{\pm}$ detection inefficiency was stable around 17 permille.

4.7 Transmission for C_6F_{14} below 190 nm

Since the PM-tubes and the active wavelength shifter PPO are not sensitive in the region below 190 nm the performance of the Cherenkov liquid in CPLEAR does not require good transmission in this region. This is,

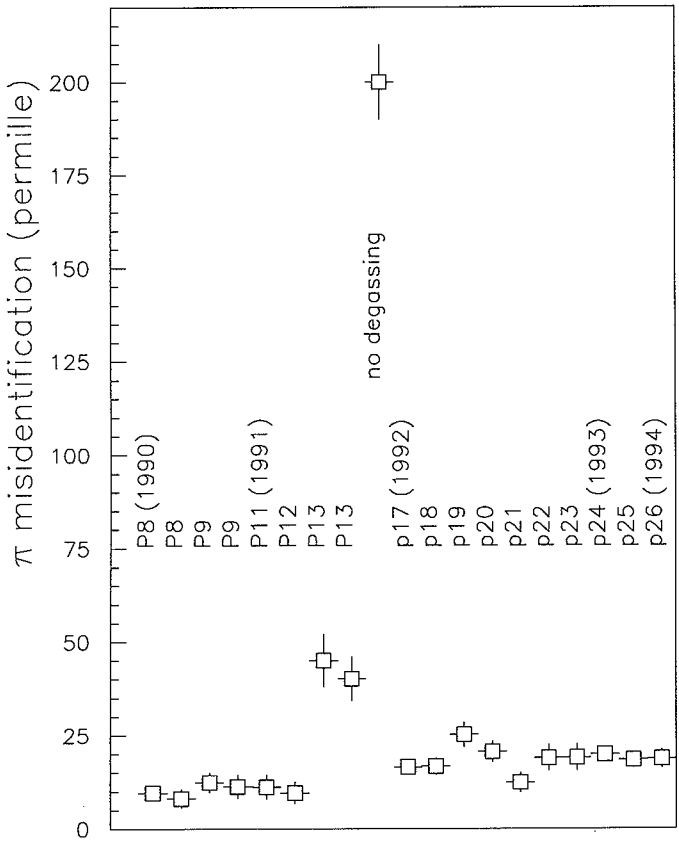

Figure 4.5: *Pion rejection inefficiency for run P8 in 1990 to P26 in 1994. The point at 200 permille indicates when the degassing was first implemented and what the inefficiency would have been without degassing.*

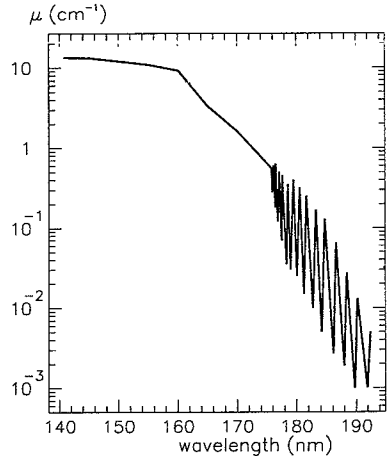

Figure 4.6: *Oxygen absorption μ versus wavelength where μ is the absorption coefficient for 1 cm of oxygen at NTP*

however, not the case for the many experiments [75, 76] that use TMAE [84] as a photon converter. The molecular absorption bands of oxygen [85] (Fig. 4.6) absorb a substantial part of the emitted Cherenkov light to which the TMAE material would be a suitable converter to electrons. In order to investigate what impact the ultrasonic treatment had on the transmission properties of the C_6F_{14} [86], a sample of 1.5 dm^3 of pure C_6F_{14} was kept in a glass bottle and put in an ultrasonic bath for 50 minutes. The liquid was then kept under an argon atmosphere to avoid re-absorption of oxygen. Afterwards the liquid was put into contact with 5 dm^3 of air and the transmission from 160 nm to 220 nm was measured [79]. The sample was after this once again exposed to ultrasound, and the transmission before and after this treatment is displayed in Fig. 4.7. It can be seen that an improvement of the transmission is achieved in the wavelength region around 170 nm. The improvement indicated in Fig. 4.7 might seem to be modest but since around 170 nm, the quantum efficiency of the TMAE is high and a significant amount of Cherenkov light is emitted this makes it important for the efficiency of a Cherenkov

counter. For example in the case of the Delphi RICH at CERN [75, 79] the number of detected photoelectrons (around 10) decrease with more than 50% for the case of oxygen saturated liquid compared to the number of detected photoelectrons for the case of liquid without oxygen [87]. The quantum efficiency of TMAE [84] is indicated in Fig. 4.7. The light below 160 nm is cut by the fused silica window used in the monochromator.

4.8 Summary

Calculating the bubble size according to eq. (4.1) and comparing the loss of efficiency with the case of leaking counters, where the amount of missing liquid has been measured after taking some counters out, indicates that the air bubbles in the Cherenkov counters would have resulted in an increase of the pion detection inefficiency of a factor 20 or more. With the help of 32 ultrasonic baths it was possible to get rid of 90 % of the bubbles and restore the pion detection efficiency to a value comparable to previous run periods. For most of the counters about 10 dm^3 of dissolved air (corresponding to 2/3 of the total air content) was forced out of the C_6F_{14}.

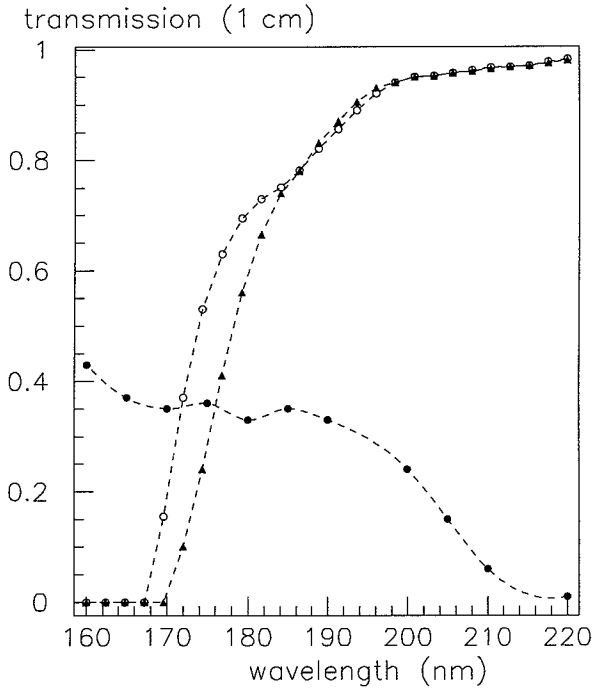

Figure 4.7: *Improvement of transmission of 1 cm C_6F_{14} by ultrasound treatment. Transmission before (▲) and after the ultrasound treatment (○). For comparison the detection efficiency of TMAE (•) according to measurements by Holroyd et al. [84] is displayed.*

Chapter 5

Data processing

The information written to tape during data taking consists for each event of coded digitized information from all the detector elements. Of these events 12% are golden and the rest comes from other annihilation channels. The background consists mainly of different pionic final states (65%) but it also contains the kaonic channels $K^{\pm}K^{\mp}\pi^{\pm}\pi^{\mp}$ (20%) and $K^{\pm}\pi^{\mp}\bar{K}^0(K^0)+\pi^0$ (5%) [66].

The data processing described in this chapter was centrally planned and organized by the collaboration as a whole and a large fraction of it was performed at CERN. The events were initially preprocessed with cuts applied to reduce the background due to non-golden annihilation channels (section 5.1). The next step is to select events with a particular decay of the neutral kaon for the different analysis groups. In our case semileptonic decays are selected and the events at this stage are referred to as super-semileptonic events (section 5.2). The result of the processing described in this chapter is used in the final semileptonic event selection (see chapter 6).

5.1 First stage of data processing

In the first stage of data processing the data is decoded to see what detector elements were hit and to get the corresponding ADC and TDC

values. The digitized values are translated to the physical values using calibration constants. Hits in the tracking system are transformed into coordinates in space. The tracks are then parameterized by a pattern recognition program that is similar to the online track follower. The kaon candidate is examined in more detail and is required to have a dE/dx signal in the PID consistent with a kaon and a momentum exceeding 350 MeV/c. The four track events must have at least two primaries and each track must have at least three DC wire hits and at least two hits in the strips for the z-coordinate. The charge of the event must be zero.

The four tracks are first fitted individually to get the track parameters. The vertex fits are performed for the tracks in all possible two by two combinations and each track pair is required to meet in space. The output from the fit is the position of the vertex and the momenta at the vertex point, together with the error matrix. There are two possible particles with opposite charge to the kaon to form the primary pair. This means there are two possible combinations of the particles. Once the correct combination is chosen, the results from the vertex fits are used to calculate the lifetime of the neutral kaon. The selection of the correct vertex combination is made by judging the χ^2 of the vertex fit, checking how well the vector of missing momentum in the primary vertex points to the secondary vertex etc. (described in detail in chapter 6.3.1).

In the first filtering, kinematic fits are performed. The number of constraints of the kinematic fits are given by the difference in the number of equations to be fulfilled and the number of quantities not measured. For example, energy and momentum conservation at the primary vertex (four equations) and the momentum of the neutral kaon (three quantities), which is not directly measured, results in a one constraint (1C) fit. To select the decay channels $K^0 \to \pi^{\pm}e^{\mp}\nu$ and $K^0 \to \pi^+\pi^-\pi^0$ (the ν/π^0 is not detected) two constraint (2C) fits are performed for demanding energy and momentum conservation for the whole event. To select $K^0 \to \pi^+\pi^-$ decays a four constraint fit (4C) is used that demands momentum conservation, or a five constraint fit (5C) is used that adds the constraint of a missing mass of a neutral kaon at the primary vertex. The output of the kinematic fits includes the probability that the assumed kinematic hypothesis is true and a set of improved variables for momenta and vertex positions that gives the maximum probability. Cuts are made on the probability but the improved values obtained from the fits are not used in the analysis presented in this thesis since the resulting improvement in

resolution does not reduce the errors in measured asymmetries (like A_T) that are not time dependent. Flags are put on each event based on the probability for the kinematic fits to indicate the decay channel for the kaon. The probability of the 1C fit is required for all events to exceed 1% for at least one of the two combinations of tracks forming the primary vertex. This cut together with the demands on the $K^{\pm}$ candidate reduces the background from non golden annihilation channels.

5.2 Super-semileptonic selection

In the super-semileptonic event selection semileptonic event candidates are separated and the number of events reduced to a number which can be handled from a practical point of view. The data should fit into a number of exabyte tapes which can be reprocessed in reasonable time. Another requirement is that the number of good semileptonic events cut at this level be negligible. These demands determine the level of the cuts described in this section.

Two further quality cuts are made. The number of hits per track in the drift chambers must be at least four and the number of hits in the strips (for z-coordinates) must be at least two. The semileptonic candidate events must fulfill the following requirements:

1. From the PID signals at least one of the tracks must have a probability of less than 5% of being a pion.
2. In the 1C fit the event must have a probability larger than 5% OR the event must be recognized as a semileptonic event by the neural networks described in section 6.
3. In the 2C fit the event must have a probability of greater than 5% OR the event must be recognized as a semileptonic event by the neural networks described in section 6.

The number of semileptonic events finally selected (see chapter 6) is around 1/20 of the number of super-semileptonic events selected at this stage.

5.3 Monte Carlo simulation

The CPLEAR Monte Carlo detector simulation program CPGEANT [88] is a modified version of the GEANT 3.15 program [89] that was tailored for the CPLEAR detector efficiency and geometry. In CPGEANT one selects the annihilation channels and decays that one wants to simulate. The Monte Carlo (MC) program for detector simulation includes an event generator for each annihilation channel taking into account the available phase space. For each particle, energy loss and scattering in the detector is taken into account. The responses of the subdetectors in terms of inefficiencies and resolutions are simulated to obtain the ADC and TDC values described in section (3). The simulation of the trigger is done by a special simulation package [90] and each event is required to pass all trigger stages described in section 3.6. The MC generated data is passed through the same filtering as the real data. The format of the MC data is the same as for the real data except that the input to the simulation (true values) for quantities like momenta etc is stored together with the output from the simulation.

The MC is tuned mainly with minimum bias data. The resolution of the drift chambers can, for example, be obtained from back to back tracks from $p\bar{p} \to \pi^+\pi^-$ The inefficiency of the tracking system is obtained from the hit probability for tracks in minimum bias data.

For the analysis in this thesis simulations of the following decay modes of the neutral kaon have been used:

- $K^0(\overline{K^0}) \to \pi^{\pm}e^{\mp}\nu$
- $K^0(\overline{K^0}) \to \pi^{\pm}\mu^{\mp}\nu$
- $K^0(\overline{K^0}) \to \pi^{\pm}e^{\mp}\nu$ where the neutral kaon was created through the annihilation channel $p\bar{p} \to K^{\pm}\pi^{\mp}(K^0)\overline{K^0}\pi^0$ with an extra π^0 at the primary vertex.
- $K^0(\overline{K^0}) \to \pi^+\pi^-$
- $K^0(\overline{K^0}) \to \pi^+\pi^-\pi^0$

Chapter 6

Analysis of semileptonic events

In section 6.1 the goals of the analysis are discussed, in section 6.2 some theory behind the neural networks used for event selection is given while in section 6.3 the analysis is described. The cuts on the data are motivated and a comparison of data and MC is made when all cuts have been implemented. The amount of remaining background is listed in section 6.4. Finally, in section 6.5 the normalization of the data is described.

6.1 Aim of analysis

After the initial data processing and the super semileptonic event selection the sample consists of 95% of background, mainly from $K^0(\overline{K^0}) \to \pi^+\pi^-$, and only of the order 0.5% of $K^0(\overline{K^0}) \to \pi^+\pi^-\pi^0$. If one disregards a small fraction of events with γ conversions ($\gamma \to e^+e^-$) and possible residual background from other annihilation channels, the rest of the events contribute to the signal. The signal can in turn be divided into 50% $K^0(\overline{K^0}) \to \pi^\pm e^\mp \nu$, 30% $K^0(\overline{K^0}) \to \pi^\pm \mu^\mp \nu$ and 20% $K^0(\overline{K^0}) \to \pi^\pm e^\mp \nu$ where the neutral kaon was created through the annihilation channel $p\bar{p} \to K^\pm\pi^\mp(K^0)\overline{K^0}\pi^0$ with an extra π^0 at the primary vertex. The $K^0(\overline{K^0}) \to \pi^\pm\mu^\mp\nu$ contributes to the signal since only the charge of the

lepton is important in the semileptonic asymmetries. For the semileptonic events with an extra π^0 at the primary vertex the calculated lifetime for the neutral kaon gets distorted. The lifetime resolution is important for time dependent asymmetries like eq. (2.42) but not for the flat asymmetries defined according to eq. (2.39) and eq. (2.40).

Since the semileptonic events only constitute a few percent of all events, one challenge in the semileptonic analysis is to select the semileptonic events with a high efficiency while at the same time reducing the background. The main background processes are the neutral kaon decays into $\pi^+\pi^-$ and $\pi^+\pi^-\pi^0$. Since the energy and momentum of the ν in $K^0(\overline{K^0}) \to \pi^\pm e^\mp \nu$ are not measured, it is difficult to distinguish the different channels. In particular the $K^0(\overline{K^0}) \to \pi^+\pi^-$ background is severe since the ratio of K_S/K_L decaying inside the detector is around 15. As an example of the problem, with a typical error in momentum for the charged tracks of around 30 MeV/c, the invariant mass distributions (assuming $K^0(\overline{K^0}) \to \pi^\pm e^\mp \nu$) for the three different decay channels of $K^0(\overline{K^0})$ are not easily separated (Fig. 6.1). To select the events one has to make a cut in a multi-dimensional space and in this context it is advantageous to use parallel processing units in the form of artificial neural networks (ANN) [91]. Since the ANN can learn correlations between the different input variables, it can optimize the cuts in a way that one obtains an optimal signal to noise ratio [92].

Another important challenge is to correct for different detection efficiencies and interactions in the detector for particles with different charge. This influences the number of detected K^0 versus $\overline{K^0}$, as well as the number of detected neutral kaon decays into $\pi^+ e^- \nu$ versus decays into $\pi^- e^+ \nu$.

To check the systematic errors the Monte Carlo is used to indicate the impact from the different backgrounds and to exclude any large artificial bias from the trigger or event selection on the data. The measured parameters are also compared for different trigger types, different magnetic fields and different data taking periods. To check the sensitivity of the measured parameters to the cuts, both an analysis with stricter cuts and one with looser cuts were performed.

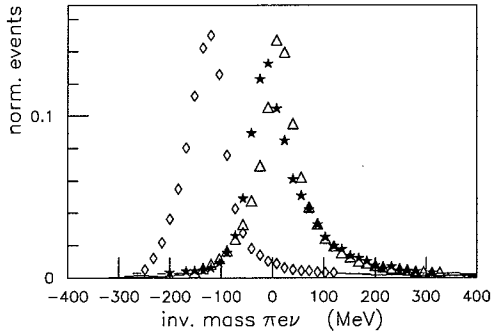

Figure 6.1: *Invariant mass distribution (assuming $K^0 \to \pi^{\pm}e^{\mp}\nu$) for the MC generated channels $K^0 \to \pi^{\pm}e^{\mp}\nu$ ($\triangle$), $K^0 \to \pi^+\pi^-$ ($\star$) and $K^0 \to \pi^+\pi^-\pi^0$ ($\diamond$) where the mass of the neutral kaon has been subtracted. Each distribution has been normalized to have an area equal to unity.*

6.2 Parallel processing

In high energy physics Artificial Neural Networks (ANN) have been used mainly to identify jets [93] but it has also been implemented in searches for the Higgs boson [94]. ANN algorithms have usually been implemented in software but there are also some successful hardware applications [70, 95, 96, 97]. An important feature of a neural network is its ability to generalize. This means that it can interpolate between different vectors used for training and recognize vectors it has never seen. From my experience, a limitation of a neural network (e.g. feed forward layer network trained with back propagation) is its inability to learn the features of a small subsample (1%) of the whole sample when this is exceptional in some way. This means that it will not recognize a small subgroup of good events, so if something is wrong with only a few events in the learning sample it might not have a significant impact on the per-

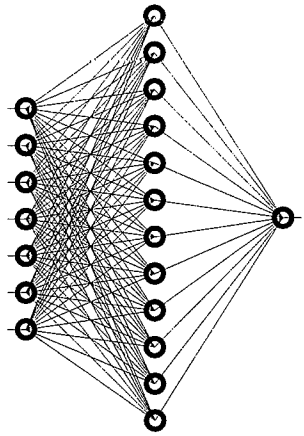

Figure 6.2: *Design of ANN_{vert}, $ANN_{\pi^+\pi^-}$ and $ANN_{\pi^+\pi^-\pi^0}$. To the left the seven input neurons are showed, the hidden layer in the middle contains twelve neurons while the single output neuron is indicated to the right. There is one weight for each connection between the neurons, where the connections are drawn here as lines. The weights are adjusted during the training to optimize the separation between different classes of events*

formance of the trained network. In the application here, first an ANN (denoted ANN_{vert}) with seven inputs selects the correct combination of tracks for the primary and secondary vertex. Secondly, for the selection of the electron an ANN (denoted ANN_{PID}) has been trained to recognize electrons from the dE/dx and TOF values measured by the PID [98]. Thirdly, the semileptonic events are separated from the background channels $K^0 \to \pi^+\pi^-$ and $K^0 \to \pi^+\pi^-\pi^0$ using two other ANN (denoted $ANN_{\pi^+\pi^-}$ and $ANN_{\pi^+\pi^-\pi^0}$, respectively) with kinematic input variables. Section 6.3 will give a detailed description of the inputs to all these networks.

The ANN_{vert}, $ANN_{\pi^+\pi^-}$ and $ANN_{\pi^+\pi^-\pi^0}$ Fig. 6.2 networks each consists of seven inputs and twelve neurons in one hidden layer. Vari-

ation of the network, like more or less neurons in the hidden layer or another hidden layer, resulted in equal or worse performance. The transfer functions in the neurons are tangent hyperbolicus and the output node is trained to be +0.8 for good events and -0.8 for bad events. Using (-0.8,0.8) as the desired output instead of the minimum/maximum output (-1,1) facilitates the training since the neurons are less exposed to saturation occurring in the tails of the tangens hyperbolicus. The training was performed using the back propagation (BP) algorithm [91]. In BP the root mean square of the difference between the actual output d_i and the desired output o_i of the output node defines an energy function that is minimized by changing the weights to make a gradient descent along the energy surface. The weights are changed according to:

$$w_{kj} \rightarrow w_{kj} + \delta_{ok} y_j \tag{6.1}$$

where w_{kj} is the weight for the connection between neuron k and neuron j. δ_{ok} is the error

$$\delta_{ok} = \frac{1}{2}(d_k - o_k)(1 - o_k^2) \tag{6.2}$$

and y_j is the output of the neuron j in the hidden layer. For the hidden layer the error is

$$\delta_{yj} = \frac{1}{2}(1 - y_j^2) \sum_{k=1}^{12} \delta_{ok} w_{kj} \tag{6.3}$$

Before the training starts the weights are initiated to random values in the interval [-0.1,0.1]. This is a standard procedure but the interval, which influences the speed of convergence, must be chosen from case to case. What is important is that it is not much larger than the weights at the global minimum, otherwise the gradient descent minimization will not converge.

For the training of the different ANN, the MC generated events were used for the different decays of the neutral kaons. For ANN_{vert} 50% of the events were $K^0 \rightarrow \pi^+\pi^-$ and 50% were $K^0 \rightarrow \pi e \nu$, half of them with the right primary association (desired output 0.8) and the other half of them with the wrong association (desired output -0.8). The problem of associating the right track to the vertex is more difficult for $K^0 \rightarrow \pi^+\pi^-$ than for $K^0 \rightarrow \pi e \nu$ because the former mainly occurs at short lifetimes and the two vertices are closer together. The proportion of

different classes of events to recognize in the training sample should be roughly the same [99]. All in all the training sample contained 10000 events. After some 40000 training presentations (5000 epochs[1]) it was not possible to further improve the performance of the network in terms of correct primary associations when tested on a sample independent from the training sample.

For training of $ANN_{\pi^+\pi^-}$ 50% of the events were $K^0 \to \pi^\pm e^\mp \nu$ and 50% were $K^0 \to \pi^+\pi^-$, while for $ANN_{\pi^+\pi^-\pi^0}$ the $K^0 \to \pi^+\pi^-$ were exchanged to $K^0 \to \pi^+\pi^-\pi^0$. Approximately the same number of training presentations were required for $ANN_{\pi^+\pi^-}$ and $ANN_{\pi^+\pi^-\pi^0}$ as were required for ANN_{vert} until the performance did not improve further in tests on an independent sample.

6.3 Semileptonic events selection

All the cuts to select semileptonic events are listed in Table 6.1 and Table 6.2 where the fractions of events cut in each channel (according to MC) are given. The first two cuts are made on the individual tracks. The number of tracks found by the offline analysis should obviously be four for a semileptonic event and this is what the first cut requires. The second cut makes sure that there are not two particles passing through the same PID sector. This is important since the PID signals are used to identify the electron and if two particles traverse the same sector the signals from the scintillators and the Cherenkov detector are not reliable. After these cuts primary and secondary vertex are selected and one cut is made on the lifetime of the neutral kaon and a number of cuts to get rid of badly reconstructed events. One of the secondaries is then demanded to be recognized as an electron and the rest of the cuts are made exclusively to reduce the backgrounds.

The analysis has been performed with two different sets of cuts, referred to as "strict cuts" and "loose cuts". The reason to use two sets of cuts is that this gives the opportunity to check if there are any systematic differences in the results (see section 7) for the two cases. The difference between the strict cuts and loose cuts is the following:

[1]The weights are only updated after accumulating the results over one epoch of training presentations, in this case after eight training presentations

- The cut on the difference between the closest approach of the track (when fitted individually) to the vertex is changed from 2 *cm* for strict cuts to 6 *cm* for loose cuts.

- The 1C probability is demanded to be larger then 0.1 for strict cuts while for loose cuts it is demanded to be larger than 0.01.

- The 2C probability (with $K^0(\overline{K^0}) \rightarrow \pi^{\pm}e^{\mp}\nu$ hypothesis) is demanded to be greater than 0.1 for strict cuts while for loose cuts there is no demand.

The loosening of the cuts mainly causes an increase in the number of semileptonic decays where an additional π^0 was present at the primary vertex. Those events will pass if the 1C and 2C probability cuts are relaxed. The 1C fit probability cut is not put to zero since there is a cut on the 0.01 level already at earlier filter stages, demanding that at least one of the combinations of primaries pass. The increase in number of events for loose cuts is around 50%.

6.3.1 Assignment of tracks to vertices

The first problem in the analysis is to find which of the four tracks are primary and which are secondary. The $K^{\pm}$ is identified with a very high certainty and the fraction of misidentified $K^{\pm}$ is less then 1/10000 [66, 67]. Thus the problem consists of combining $K^{\pm}$ with the right track, out of two possible tracks with opposite charge to the $K^{\pm}$, to form the primary vertex.

The following quantities contain valuable information when determining which track to associate to which vertex and are used as inputs to ANN_{vert} which is taught to recognize the correct association:

1. Sum of χ^2 for primary and secondary vertex fits.

2. Difference in χ^2 of vertex fit for the two combinations. The absolute number of this quantity is the same for the two combinations but the sign is different.

Cut	$\pi^{\mp}e^{\mp}\nu$	$\pi^0 + \pi^{\pm}e^{\mp}\nu$	$\pi\mu\nu$	$\pi^+\pi^-$	$\pi^+\pi^-$
no. of tracks in pattern = 4	6.8%	7.5%	5.8%	6.0%	6.2%
max. one track per PID sector	6.6%	7.2%	7.7%	1.7%	12.2
ANN_{vert} output difference ≥ 0.1	2.0%	6.3 %	1.9%	7.1%	1.5 %
K^0 lifetime $\geq 2\ \tau_s$	11.9%	15.7%	9.1%	76.8%	9.2 %
distance between vertex and track ≤ 2 cm	15.7%	16.3%	18.0%	27.4%	20.7%
sum of χ^2 for prim. and sec. vertex ≤ 15	10.0%	12.0%	12.5%	8.9%	14.3
distance between vertices ≥ 1 cm	0.1%	0.1 %	0.1%	1.6%	0.1 %
1C prob ≥ 0.1	9.9%	72.4%	10.8%	9.9%	11.2%
primary vertex inside target	0.6%	1.7%	0.8%	0.7%	0.2%
one electron	37.6%	40.0 %	84.3 %	94.7%	85.0%
$ANN_{\pi^+\pi^-}$ rejection	17.7%	13.1%	15.8%	89.1%	9.0%
$ANN_{\pi^+\pi^-\pi^0}$ rejection	6.3%	8.9%	29.8%	8.2%	91.4%
2C prob ≥ 0.1	6.5%	67.7%	10.7%	19.6%	24.5
$30° \leq$ secondary op. angle $\leq 150°$	3.6%	3.1%	4.3%	6.7%	14.7%
$25° \leq$ primary op. angle $\leq 170°$	1.5%	1.1%	1.7%	2.4%	1.7%
matching of tracks in pattern and trigger	1.1%	6.5%	1.0%	2.4%	0.9%

Table 6.1: *Fraction of events cut in each channel at each step referring to remaining events after previous step for strict cuts*

3. The square of the missing mass at the primary vertex subtracted with the square of m_{K_0}.

4. The angle between the missing transverse momentum for the K^0 and the vector from the primary to secondary vertex in the transverse plane.

5. Same but in three dimensions.

6. Error in momentum for $K^{\pm}$.

7. Same for associated primary track.

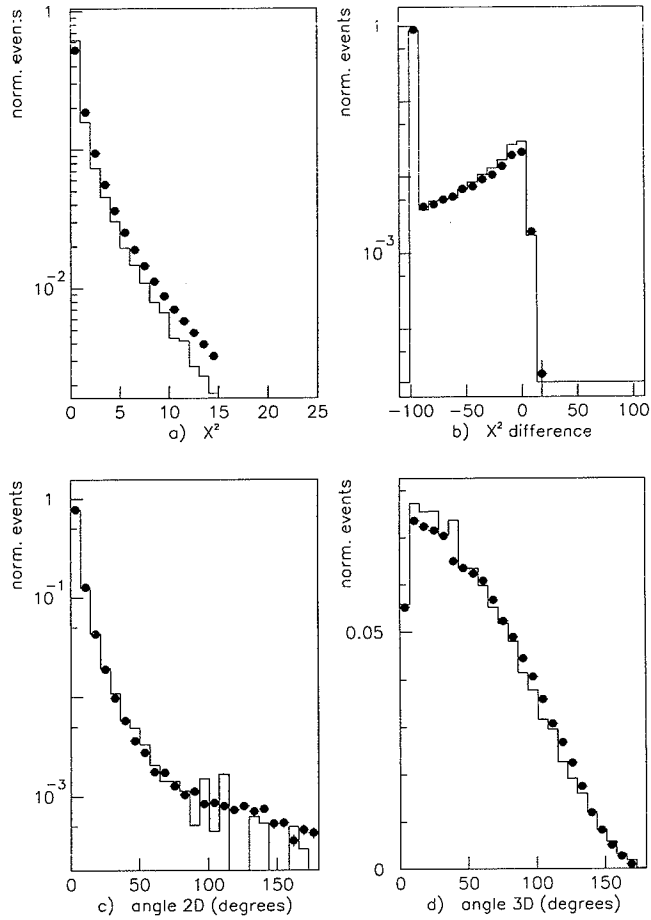

Figure 6.3: *Input variables for ANN_{vert} after strict cuts for data (solid line) and MC (•) where expected background is included in the MC. The number of events has been normalized to unity area for all distributions: a) sum of χ^2 for vertex fits b) difference in χ^2 of vertex fit for the two combinations c) alignment of missing momentum for K^0 with the vector from primary to secondary vertex in the transverse plane (2D) d) alignment of missing momentum for K^0 with the vector from primary to secondary vertex in 3 dimensions (3D)*

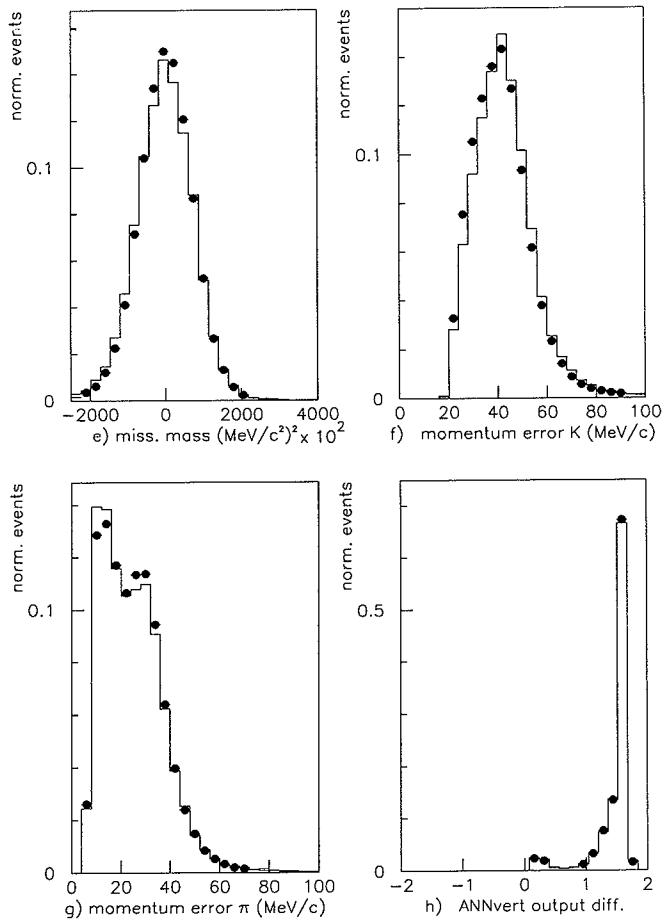

Figure 6.3: *e) the square of the missing mass at the primary vertex subtracted with the square of m_{K_0} f) error in momentum for $K^{\pm}$ g) error in momentum for associated primary $\pi^{\pm}$ h) difference of ANN_{vert} output for the two possible combinations.*

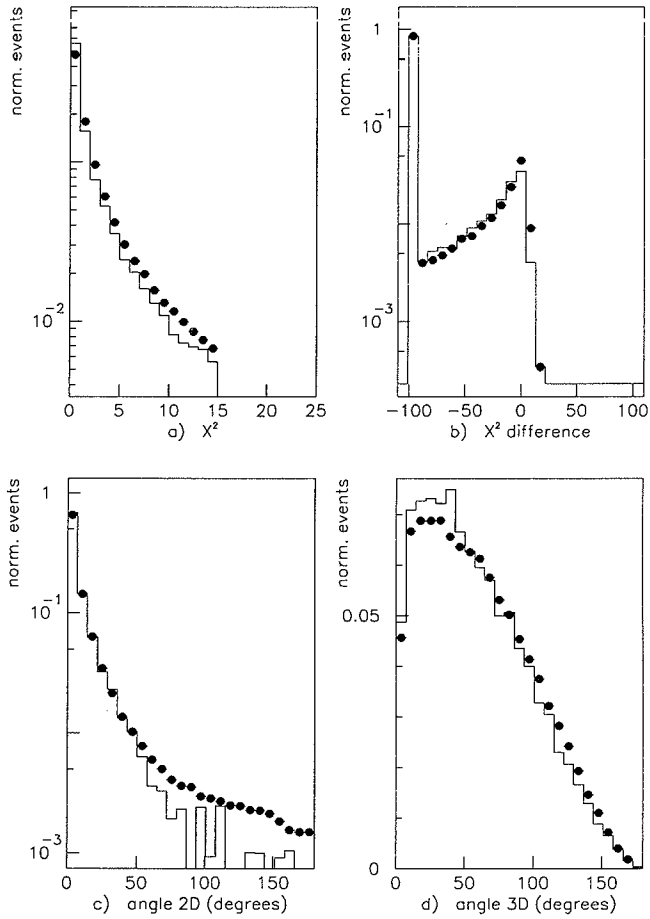

Figure 6.4: *Input variables for ANN_{vert} after loose cuts for data (solid line) and MC (•) where expected background is included in the MC. The number of events has been normalized to unity area for all distributions: a) sum of χ^2 for vertex fits b) difference in χ^2 of vertex fit for the two combinations c) alignment of missing momentum for K^0 with the vector from primary to secondary vertex in the transverse plane (2D) d) alignment of missing momentum for K^0 with the vector from primary to secondary vertex in 3 dimensions (3D)*

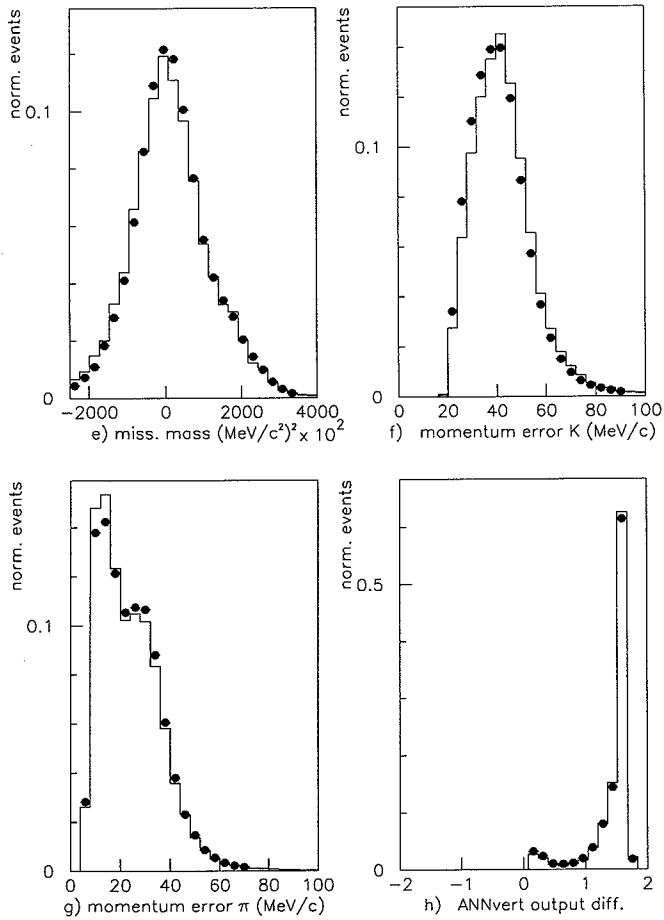

Figure 6.4: *e) the square of the missing mass at the primary vertex subtracted with the square of m_{K_0} f) error in momentum for $K^{\pm}$ g) error in momentum for associated primary $\pi^{\pm}$ h) difference of ANN_{vert} output for the two possible combinations.*

Cut	$\pi^{\pm}e^{\mp}\nu$	$\pi^0 + \pi^{\pm}e^{\mp}\nu$	$\pi\mu\nu$	$\pi^+\pi^-$	$\pi^+\pi^-\pi^0$
no. of tracks in pattern = 4	6.8%	7.5%	5.8%	6.0%	6.2%
max. one track per PID sector	6.6%	7.2%	7.7%	1.7%	12.2 %
ANN_{vert} output difference ≥ 0.1	2.0%	6.3 %	1.9%	7.1%	1.5 %
K^0 lifetime $\geq 2\ \tau_s$	11.9%	15.7%	9.1%	76.8%	9.2 %
distance between vertex and track ≤ 6 cm	5.2%	5.3%	6.5%	10.7%	8.5
sum of χ^2 for prim. and sec. vertex ≤ 15	13.0%	14.9%	16.7%	17.1%	18.9 %
distance between vertices ≥ 1 cm	0.1%	0.1 %	0.1%	1.6%	0.1 %
1C prob ≥ 0.01	0.9%	34.6%	1.6%	1.5%	2.4 %
primary vertex inside target	0.6%	1.7%	0.8%	0.7%	0.2%
one electron	37.6%	40.0%	84.3%	93.8%	79.0%
$ANN_{\pi^+\pi^-}$ rejection	10.7%	9.5%	8.1%	78.8%	4.0%
$ANN_{\pi^+\pi^-\pi^0}$ rejection	6.5%	7.5%	29.5%	10.1%	90.5%
$30° \leq$ secondary op. angle $\leq 150°$	4.0%	5.2%	4.3%	5.6%	17.1%
$25° \leq$ primary op. angle $\leq 170°$	1.5%	0.9%	1.9%	1.2%	2.5%
matching of tracks in pattern and trigger	1.0%	5.8%	1.1%	1.2%	1.0%

Table 6.2: *Fraction of events cut in each channel at each step referring to remaining events after previous step for loose cuts*

The distributions of the variables listed above are plotted in Fig. 6.3 and Fig. 6.4 for the correct combination. The plots are produced after all cuts have been made according to Table 6.1- 6.2 and the cuts are strict for Fig. 6.3 while they are loose for Fig. 6.4. Data and MC are plotted overlayed and the agreement is generally good, even if some deviations in the tails as for example in the χ^2 (Fig. 6.3a and 6.4a), can be seen. The most important input variables to the ANN_{vert} are the first three in Fig. 6.3 and Fig. 6.4. For the cases where the vertex fit does not converge, the difference between the χ^2 for the two possible vertex combinations is put to 100, e.g. for all events with only two primary tracks, where the decay took place outside PC2. For these events the association of a track to the vertex is trivial and in Fig. 6.3b and Fig. 6.4b these events are gathered in the peak at -100. Although the ANN classifies these events

correctly, they are not treated separately. The alignment of the missing momentum with the vector between the vertices is very good for the correct combination in two dimensions (Fig. 6.3c and 6.4c) while it gets smeared in three dimensions (Fig. 6.3d and 6.4d). The missing mass for the strict cuts (Fig. 6.3e) is centered around zero once the mass of the neutral kaon is subtracted. For loose cuts (Fig. 6.4e) there is an increase at large missing mass. This is due to some 20% (see Table 6.3) from the channel $p\bar{p} \rightarrow K^{\pm}\pi^{\mp}\overline{K^0}(K^0)\pi^0$. For the strict case the 1C and additional 2C fit[2] cuts (probability ≥ 0.1) remove these events. The errors in the momentum of the $K^{\pm}$ in Fig. 6.3f and Fig. 6.4f and for the primary $\pi^{\pm}$ in Fig. 6.3g and Fig. 6.4g should give information about how uncertain the ANN should be. The larger the errors are, the closer the output of the ANN (in Fig. 6.3h and Fig. 6.4h) is to zero. The structure in the distribution of the momentum error from 20 MeV/c to 40 MeV/c is due to the $K^*(\overline{K^*}) \rightarrow K^{\pm}\pi^{\mp}$ coming from the golden channel in which the neutral kaon was produced through $p\bar{p} \rightarrow K^*(\overline{K^*})\overline{K^0}(K^0)$. The momentum spectrum for this (two body) channel has a distinct peak and this is reflected in the distribution of the error in momentum. Most of the outputs of ANN_{vert} are close to the desired values [-0.8,0.8] and the difference of the output for the two combinations (Fig. 6.3h and Fig. 6.4h) is usually close to 1.6 . Only a few events are below 1.0 . The events below 1.0 have in common that the χ^2 difference (Fig. 6.3b and Fig. 6.4b) is positive for the correct combination and the χ^2 of the vertex fit is thus lower for the wrong assignment than for the right assignment. Since a substantial fraction of the events with an ANN_{vert} output difference for the two possible combinations close to zero had wrongly associated tracks a cut was made (Table 6.1-6.2) demanding a difference larger than 0.1 . To further reduce the number of ambiguous events and to reduce the $K^0 \rightarrow \pi^+\pi^-$ background a cut on the vertex separation of 1 cm is made.

The cut on the χ^2 of the vertex fit is intended to cut badly reconstructed events. The same is the case for the cut on the difference between the closest approach of the track (when fitted individually) to the vertex. After all cuts about 0.25% remain with wrong primary association for $K^0(\overline{K^0}) \rightarrow \pi^{\pm}e^{\mp}\nu$, $K^0(\overline{K^0}) \rightarrow \pi^{\pm}\mu^{\mp}\nu$ and $K^0(\overline{K^0}) \rightarrow \pi^{\pm}e^{\mp}\nu$ where the neutral kaon was created through the annihilation channel with an extra π^0 at the primary vertex. For $K^0 \rightarrow \pi^+\pi^-$ 9.5% remain with wrong primary association. The larger amount of primary-secondary mismatch in this case is due to the fact that the residual background generally consists

[2] As defined in chapter 5

of events with less well reconstructed tracks. Since several cuts aim at reducing the number of $K^0 \to \pi^+\pi^-$ events, those events that are badly reconstructed will have a bigger probability of passing these cuts.

6.3.2 Selection of $e^{\pm}$

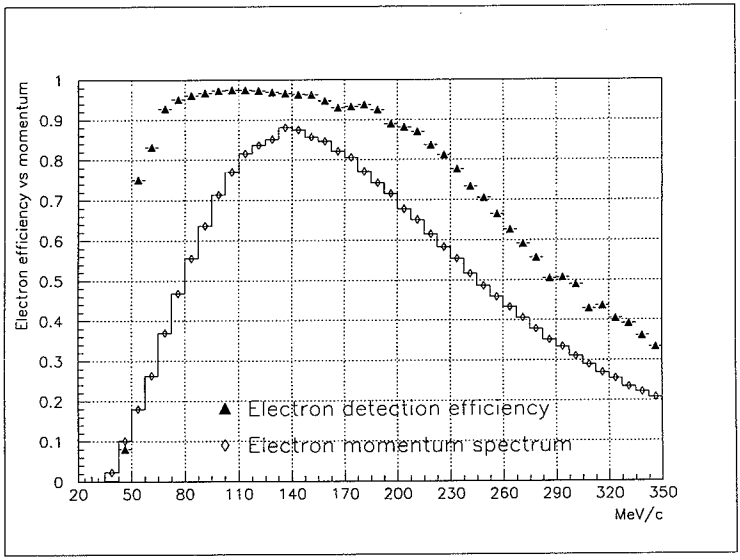

Figure 6.5: *The electron identification efficiency as a function of momentum*

After selecting primary and secondary tracks the PID information is used to insure that one of the secondaries is an electron. This is done [98] by making use of TOF, the number of photoelectrons in the Cherenkov counters and dE/dx in S1 and S2. A cut is made allowing 2% of the $\pi^{\pm}$ mesons to be misidentified as electrons. The electron identification efficiency as a function of momentum is shown in Fig. 6.5. The reason that the efficiency is decreasing for higher momenta is that the speed of the pions approaches $\beta = 1.0$, which is the β of the electrons, and also the dE/dx bands of pions and electrons merge at high momenta.

6.3.3 Background suppression

The separation of the semileptonic decays from $\pi^+\pi^-$ decays are made by $ANN_{\pi^+\pi^-}$ and the separation from $\pi^+\pi^-\pi^0$ is made by $ANN_{\pi^+\pi^-\pi^0}$.

The inputs are listed below:

1. opening angle of the secondaries in the K^0 rest frame assuming $\pi^+\pi^-$ decay
2. invariant mass of secondaries assuming $\pi e\nu$ decay - m_{K_0}
3. TOF measured for $e^\pm$ minus TOF expected assuming $\pi^\pm$
4. same assuming $e^\pm$
5. error in the momentum of the $\pi^\pm$
6. error in the momentum of the $e^\pm$
7. lifetime of neutral kaon

The distributions of these input variables, except for the lifetime of $K^0(\overline{K^0})$, are shown in Fig. 6.6- Fig. 6.7 where data and MC are plotted overlayed. The K^0 lifetime distributions are shown separately in Fig. 6.8.

The opening angle in the rest frame of the neutral kaon assuming $\pi^+\pi^-$ decay (see Fig. 6.6a and Fig. 6.7a) should be close to 180° when this decay hypothesis is true. All the events with an opening angle close to this value are cut by $ANN_{\pi^+\pi^-}$. The invariant mass distribution calculated by assuming semileptonic decays of the kaon (Fig. 6.6b and 6.7b) is very similar for $K^0 \to \pi^\pm e^\mp \nu$ decays and $K^0 \to \pi^+\pi^-$ while for $K^0 \to \pi^+\pi^-\pi^0$ (Fig. 6.1) the resulting invariant mass distribution is shifted to lower values. This variable is important to separate $K^0 \to \pi^\pm e^\mp \nu$ from $K^0 \to \pi^+\pi^-\pi^0$. The resulting invariant mass distribution after all cuts (Fig. 6.6b and Fig. 6.7b), where m_{K^0} has been subtracted, is centered around zero. The TOF measured for $e^\pm$ minus the TOF expected by assuming $\pi^\pm$ is shown in Fig. 6.6c and Fig. 6.7c while the same TOF measured for $e^\pm$ minus TOF expected by assuming $e^\pm$ is shown in Fig. 6.6d and Fig. 6.7d. It is consistent with the $e^\pm$ hypothesis. When the TOF information is

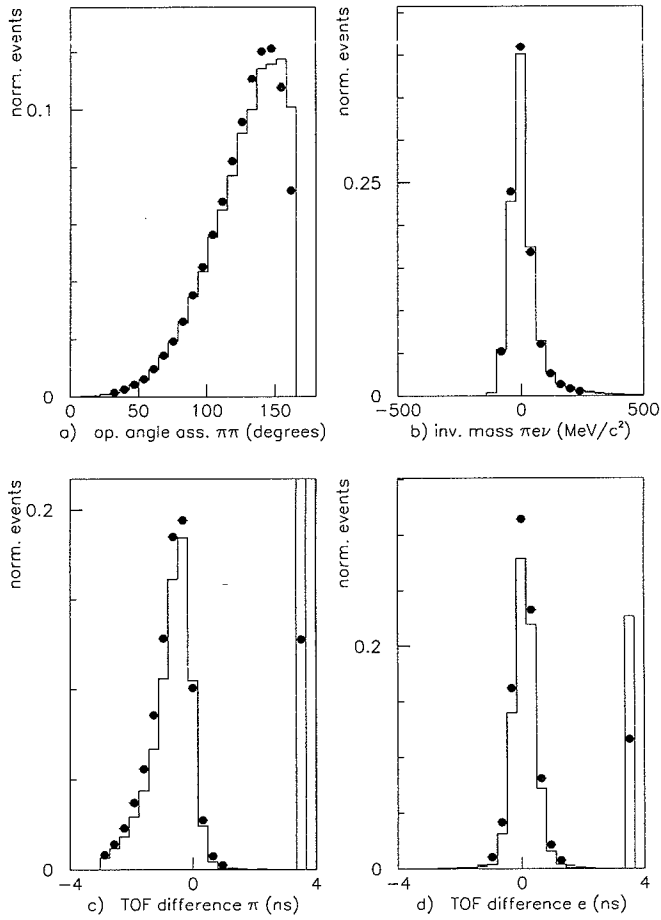

Figure 6.6: *Input variables for $ANN_{\pi^+\pi^-}$ and $ANN_{\pi^+\pi^-\pi^0}$ after strict cuts for data (solid line) and MC (•) where expected background is included in the MC. The number of events has been normalized to unity area for all distributions: a) opening angle in K^0 rest frame assuming $\pi^+\pi^-$ decay b) invariant mass assuming $\pi e\nu$ decay subtrakted with m_{K_0} c) TOF measured for $e^\pm$ minus TOF expected assuming $\pi^\pm$ d) same assuming $e^\pm$*

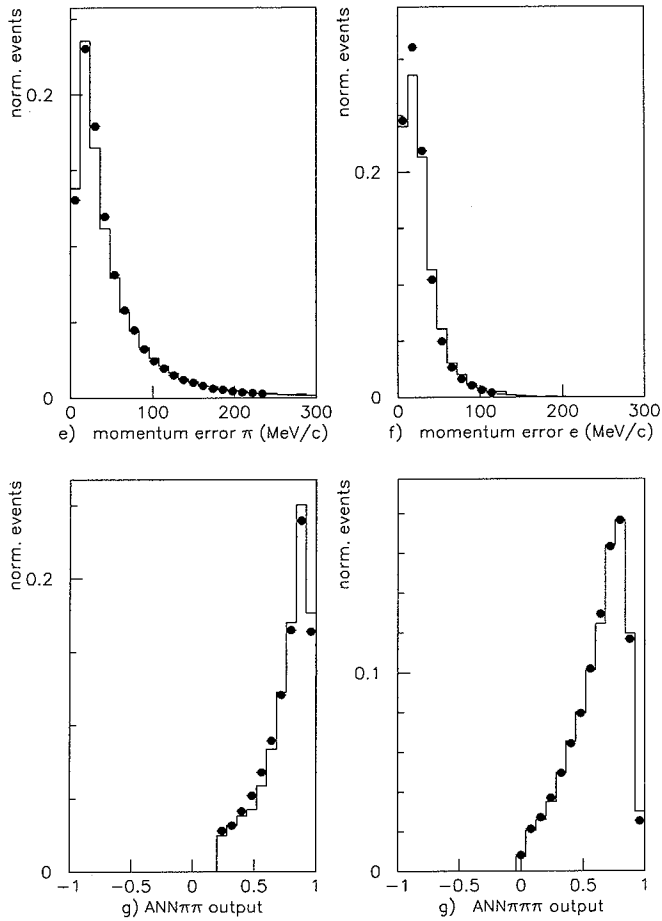

Figure 6.6: *e) error in momentum for first secondary f) same for second secondary g) output for* $ANN_{\pi^+\pi^-}$ *h) output for* $ANN_{\pi^+\pi^-\pi^0}$

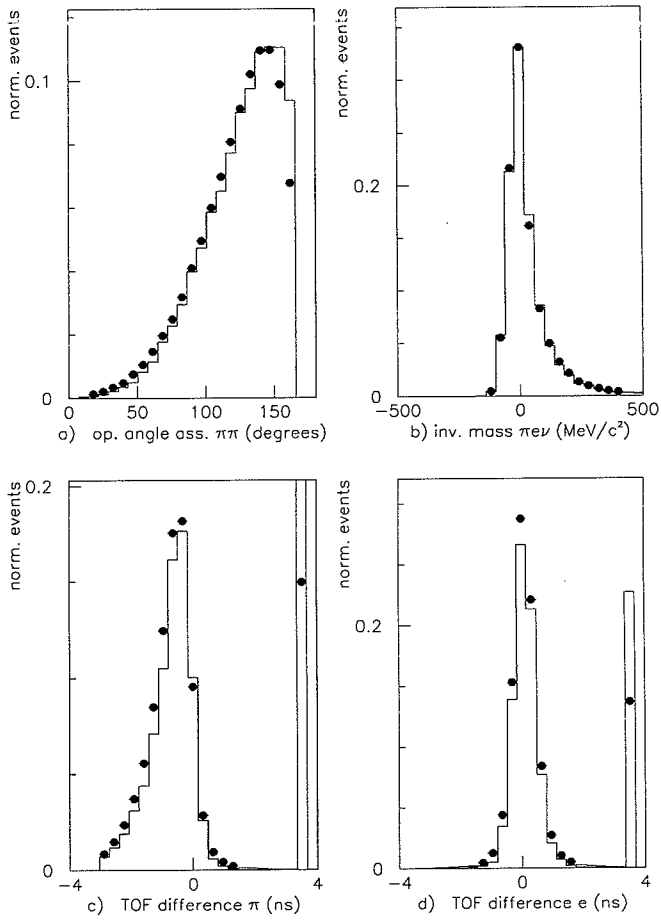

Figure 6.7: *Input variables for $ANN_{\pi^+\pi^-}$ and $ANN_{\pi^+\pi^-\pi^0}$ after loose cuts for data (solid line) and MC (•) where expected background is included in the MC. The number of events has been normalized to unity area for all distributions: a) opening angle in K^0 rest frame assuming $\pi^+\pi^-$ decay b) invariant mass assuming $\pi e\nu$ decay subtracted with m_{K_0} c) TOF measured for $e^\pm$ minus TOF expected assuming $\pi^\pm$ d) same assuming $e^\pm$*

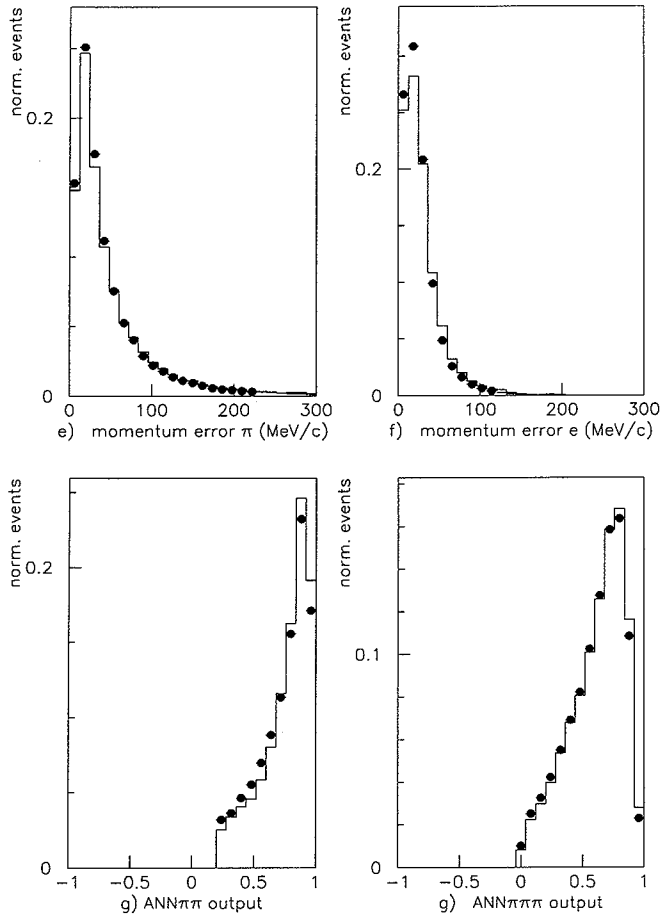

Figure 6.7: *Input variables for $ANN_{\pi^+\pi^-}$ and $ANN_{\pi^+\pi^-\pi^0}$ after loose cuts for data and MC (where MC with expected background is included) and MC is indicated with (•) e) error in momentum for first secondary f) same for second secondary g) output for $ANN_{\pi^+\pi^-}$ h) output for $ANN_{\pi^+\pi^-\pi^0}$*

missing for the electron it is put to 3.5 . This value has been chosen *adhoc* to be well away from the distribution of the difference in expected and measured TOF in order for $ANN_{\pi^+\pi^-}$ and $ANN_{\pi^+\pi^-\pi^0}$ to learn that this means no TOF information. If the TOF difference is put to 3.5 for all events, the selection efficiency decreases while the values for the parameters fitted in the asymmetries as defined in section (2.6) do not change. The distributions of the errors (Fig. 6.6e-f and Fig. 6.7e-f) are fairly similar for $\pi^{\pm}$ and $e^{\pm}$. The output of $ANN_{\pi^+\pi^-}$ and $ANN_{\pi^+\pi^-\pi^0}$ is peaked around 0.8, which is the the desired output for a semileptonic event. Since the $K^0 \to \pi^+\pi^-$ decays are more abundant than the $K^0 \to \pi^+\pi^-\pi^0$ decays, the cut on the output is made at 0.2 for $ANN_{\pi^+\pi^-}$ (Fig. 6.6g and Fig. 6.7g) while it is made at 0.0 for $ANN_{\pi^+\pi^-\pi^0}$ (Fig. 6.6h and Fig. 6.7h). The $ANN_{\pi^+\pi^-}$ cut reduces significantly the number of events at short lifetimes (Fig. 6.8). The agreement between data and MC is reasonable for the inputs and outputs of $ANN_{\pi^+\pi^-}$ and $ANN_{\pi^+\pi^-\pi^0}$ even if there is a small deviation in Fig. 6.6a and Fig. 6.7a for the opening angle above 140°.

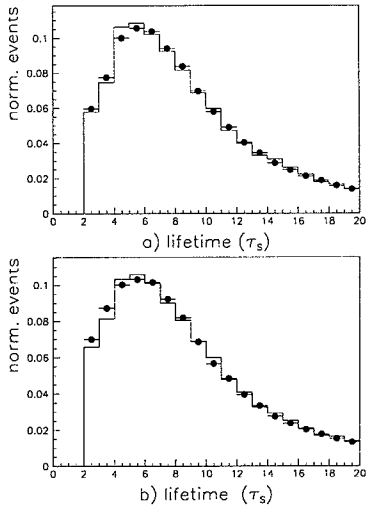

Figure 6.8: *Lifetime for the neutral kaon for data (solid line) and MC (•) after all cut have been implemented for a) strict cuts and b) loose cuts. The estimated background is included in the MC.*

Lastly the cuts on the opening angles for the primary and secondary tracks remove gamma conversions ($\gamma \rightarrow e^+e^-$) and events with back scattered particles. For the earlier data taking periods there is also, on top of the cuts in Table 6.1- 6.2, a symmetrization for HWP2. During these periods it was required that the primaries with opposite charge to the kaon must clearly not be a kaon judging the dE/dx signals etc in HWP2 as described in section (3.6.5). Since the $e^{\pm}$ is closer to minimum ionizing than the pion, events with opposite charge for electron and kaon had larger probability of passing the trigger compared to the case when the charge of electron and kaon is the same. This has been corrected for by imposing the same cut on the primaries with the same charge as the kaon and thus symmetrizing the acceptances for $K^{\pm}e^{\pm}$ and $K^{\pm}e^{\mp}$ type of events. This reduces the data by about 10% for these periods.

6.4 Amount of data and backgrounds

channel	$\pi^{\pm}e^{\mp}\nu$ (e as π)	$\pi^0 + \pi^{\pm}e^{\mp}\nu$	$\pi^+\pi^-$	$\pi^+\pi^-\pi^0$	$\pi^{\pm}\mu^{\mp}\nu$	$\pi^{\pm}\mu^{\mp}\nu$ (μ as π)
strict cuts (4P)	0.47%	2.5%	19.1%	0.07%	9.3%	1.3%
strict cuts (2P)	1.95%	3.2%	9.1%	0.61%	13.4%	3.2%
loose cuts (4P)	0.53%	24.4%	19.1%	0.18%	10.7%	1.4%
loose cuts (2P)	2.07%	14.7%	7.96%	0.73%	13.64%	2.9%

Table 6.3: *Remaining backgrounds for each channel as fraction of* $K^0 \rightarrow \pi^{\pm}e^{\mp}\nu$ *according to the MC for two primary (2P) and four primary (4P) events*

After the cuts the remaining background according to the MC is distributed according to Table 6.3. The data in this report is from P17 to P26, i.e. from data taking in 1992 to 1994 . Altogether there are around 560000 events for the alternative with the stricter cuts where 138000 events have been recorded with three or four primary tracks in the trigger while 423000 are events with two primary tracks. For the looser cuts there are 580000 two primary track events and 248000 four primary track events, which together make 829000 events. This is equivalent to an increase in the number of events of 50% by using loose cuts

as compared to using strict cuts.

When fitting the asymmetries (Chapter 7) the theoretical rates in eq. (2.38) are corrected for these backgrounds using the acceptance and shape for each background as obtained from MC.

6.5 Normalization

6.5.1 K^0 versus $\overline{K^0}$

To be able to measure a significant difference from zero of the order $2Re(\epsilon_L)$ in, for example, the A_{CPT} asymmetry eq. (2.40) one needs to know the relative flux of K^0 and $\overline{K^0}$ to an accuracy of better than $\sim 0.2\%$. There are two reasons for detecting different numbers of K^0 and $\overline{K^0}$ in CPLEAR due to the tagging of $K^0(\overline{K^0})$ using the primary $K^{\pm}\pi^{\mp}$ pair:

1. Differences due to different interaction cross sections in the detector material.
2. Geometrical differences, i.e. differences arising from the opposite curvatures of the accompanying charged particles.

An example of the former is the difference in interaction cross-section for π^+ and π^- due to different probabilities, e.g. to form the Δ resonance, and an example of the latter is the p_T cut (see section 3.6) which will act differently on K^+ and K^- since they have opposite curvature and DC1 and DC6 are not perfectly aligned.

The second effect, of the order of 1%, cancels out if one mixes the same amount of M1 and M2 data. The first effect (around 13%) is corrected for by a look up table (LUT) with $12 \times 12 \times 12$ bins [100]. Each bin in the LUT is an estimate of the $K^0/\overline{K^0}$ ratio, that can be parameterized by the three variables: total pion momentum, transverse $K^{\pm}$ momentum and the z-component of the $K^{\pm}$ momentum. The entries of the LUT are determined by selecting $K^0(\overline{K^0}) \to \pi^+\pi^-$ at short lifetimes (below 4 τ_S) by way of a 5C fit[3]. The very small CP-violation effects for such short

[3]As defined in section 5

lifetimes are corrected for assuming PDG values [29] for the CP violation. The parameters of the LUT parameterize the momentum and the amount of matter the $K^{\pm}$ passes through. The data is corrected using the LUT on an event by event basis. The momentum spectrum for the neutral kaons after the LUT correction and after all cuts have been implemented is shown in Fig. 6.9 where the spectrum of $\overline{K^0}$ is plotted overlayed with the spectrum of K^0 for strict and loose cuts. The agreement between the spectra is good and this gives confidence in the normalization method.

The normalization scheme is valid for any difference in the flux of K^0 and $\overline{K^0}$ and a possibility to check that it works as anticipated is to use it for MC. The LUT is then built by using $K^0 \to \pi^+\pi^-$ decays and this is used to normalize the semileptonic MC events. This gives a possibility to exclude any large biases on the measured physics parameters from the trigger, normalization or event selection.

6.5.2 π^+e^- versus π^-e^+

An estimation of the relative detection efficiency $\eta = \frac{\epsilon(\pi^+e^-)}{\epsilon(\pi^-e^+)}$ for the secondaries can be made from calibration data. A pure sample of electrons may be obtained by selecting photon conversion events $\gamma \to e^+e^-$. This is done by asking for an opening angle less than 5°. A sample of pions is also selected [82] from minimum bias data, i.e. data recorded with a trigger only demanding an S1 hit. In both cases the efficiency is equal for positive and negative particles within 1%. These sets of calibration data have been used to tune the MC response of the PID. The Monte Carlo can, however, currently not be used to predict η. For example, a good calibration data sample of $\mu^{\pm}$ is missing.

The most reliable way of determining η in CPLEAR is to use the world average for the charge asymmetry δ in eq. (2.41), which has been accurately measured for K_L. Fixing $2Re(\epsilon_L)$ to 0.00327 [29], the δ asymmetry can be fitted with the theoretical rates in eq. (2.38). The parameter η is included in the fit by multiplying $\overline{R}^-$ and R^- with η.

The other asymmetries are fitted, one at a time, together with δ. In this way correlations between η and the other fitted parameters are properly taken into account. The obtained value for η does not depend signif-

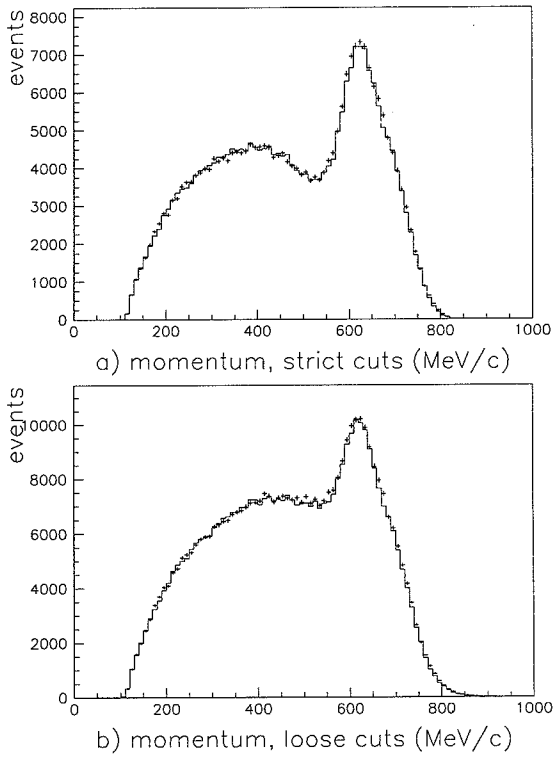

Figure 6.9: *Momentum spectrum after all cuts have been implemented for K^0 and for $\overline{K^0}$ where K^0 is indicated with the solid line and $\overline{K^0}$ with symbols. The error bars for K^0 are not given but are of the same magnitude as for $\overline{K^0}$. The momentum spectra for strict cuts are plotted in a) while the spectra for loose cuts are plotted in b).*

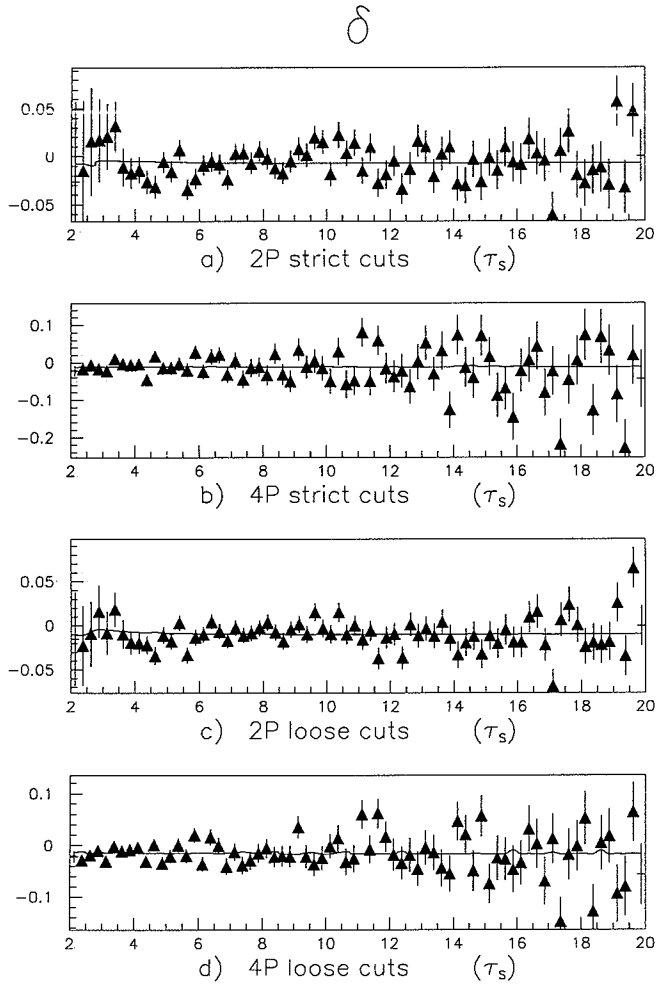

Figure 6.10: *Fit of δ from 2 τ_S to 20 τ_S (together with the A_T asymmetry) for the 2 primary (2P) and 4 primary (4P) trigger alternatives for strict and loose cuts. The fitted line is defined according to the semileptonic rates in (2.38) and eq. (2.41) assuming $\Delta S = \Delta Q$. The results are:*
a) $\eta = 1.019 \pm 0.004 \quad \chi^2 = 179/142 d.o.f.$
b) $\eta = 1.029 \pm 0.006 \quad \chi^2 = 196/142 d.o.f.$
c) $\eta = 1.025 \pm 0.003 \quad \chi^2 = 202/142 d.o.f.$
d) $\eta = 1.040 \pm 0.005 \quad \chi^2 = 203/142 d.o.f.$

icantly on which of the asymmetries A_T (eq. (2.39)), A_{CPT} (eq. (2.40)) or Δm (eq. (2.42)) that is fitted together with δ. The uncertainty in the world average value for δ of ± 0.00012 [29] is taken into account as a systematic error.

In Fig. 6.10 the fit of the δ asymmetry (together with A_T) is shown for strict and loose cuts and for the different trigger types. The resulting values for η in the case of loose cuts are $\eta = 1.025 \pm 0.003$ for events with two primaries while $\eta = 1.040 \pm 0.005$ for four primary events. For strict cuts the value for η is slightly lower, $\eta = 1.019 \pm 0.004$ and $\eta = 1.029 \pm 0.006$ for two and four primary events, respectively. The corresponding values of $Re(\epsilon_T)$ are given in section 7. The reason why η is higher for four primaries is that in this case the trigger (HWP2) requires that at least one of the pions has a signature in the PID not similar to a kaon. Since we know that a π^- has a slightly larger probability than a π^+ of giving no signal in the Cherenkov [82], events with $\pi^- e^+$ as secondaries will have a larger probability to be cut as compared to events with $\pi^+ e^-$.

The possibility in the future of determining η using calibration data and a well tuned Monte Carlo should not be excluded. This determination would in that case be an additional cross check.

Chapter 7

Results

7.1 A_T and A_{CPT}

The asymmetries A_T (2.39) and A_{CPT} (eq. 2.40) are fitted one at a time simultaneously with the asymmetry δ (eq. 2.41) using the theoretical expressions for the semileptonic rates as defined in eq. (2.38). The fitted parameters are $Re(\epsilon_S)$ and η in both cases. From the obtained value for $Re(\epsilon_S)$ the values for $Re(\epsilon_T)$ and $Re(\delta_{CPT})$ are given through eq. (2.22) and eq. (2.23) In the fit $\Delta S = \Delta Q$ is assumed and the parameter x in eq. (2.38) is put to zero. For the fit of A_{CPT} and δ also $Im(\delta_{CPT})$ is put to zero. This is justified by the fact that the sensitivity of the asymmetries to these parameters is negligible if they are varied in a reasonable interval.

The fitting procedure might seem complicated, but the important thing in the time independent asymmetries A_T (and the almost time independent A_{CPT}) is the absolute level in terms of deviation from zero after correcting for the detection efficiency η. The parameterization (in our case $Re(\epsilon_T)$ and $Re(\delta_{CPT})$) of this deviation is arbitrary.

The results obtained for strict and loose cuts for the 2 primary and 4 primary trigger cases are shown for the different data taking periods in Fig. 7.1 for $Re(\epsilon_T)$ and $Re(\delta_{CPT})$. The obtained values for $Re(\epsilon_T)$ and $Re(\delta_{CPT})$ are 40% correlated because the same δ asymmetry is used in both cases to determine η. The data taking period denoted P17 took place

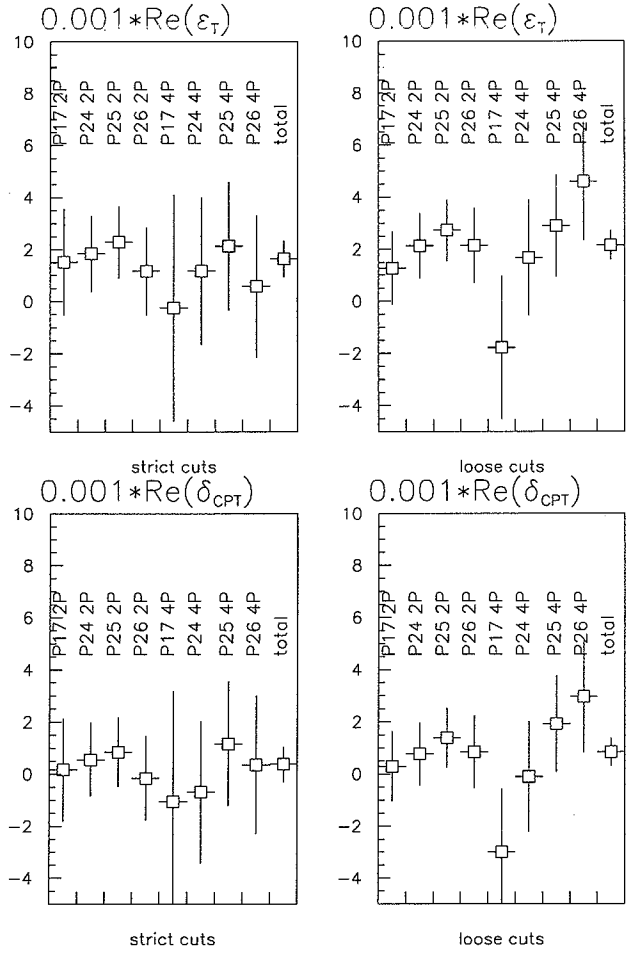

Figure 7.1: *Results for A_T and A_{CPT} in terms of $Re(\epsilon_T)$ and $Re(\delta_{CPT})$ for the 2 primary (2P) and 4 primary (4P) trigger alternatives for strict and loose cuts and different data taking periods. The data taking periods are from P17 in (1992) to P26 in (1994)*

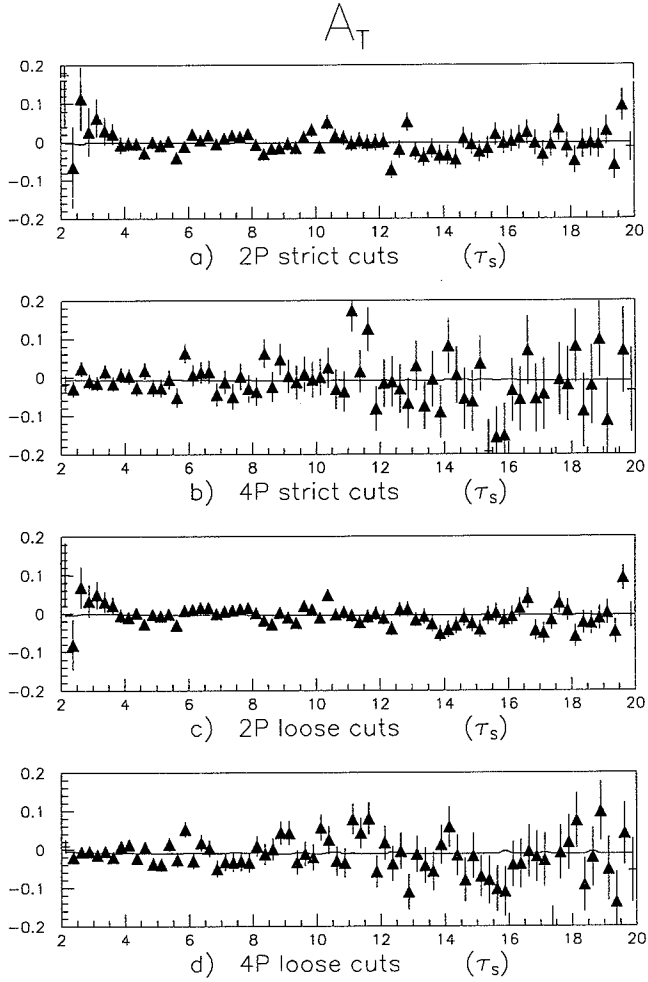

Figure 7.2: *Fit of A_T from 2 τ_S to 20 τ_S (together with the δ asymmetry) for the 2 primary (2P) and 4 primary (4P) trigger alternatives for strict and loose cuts. The fitted line is defined according to the semileptonic rates in (2.38) and eq. (2.39) assuming $\Delta S = \Delta Q$. Note that the data is not corrected for η and since this is taken into account in the fit the level of the line is not equal to $4Re(\epsilon_T)$. The results are:*
a) $Re(\epsilon_T) = (1.8 \pm 0.8) \cdot 10^{-3}$ $\chi^2 = 179/142 d.o.f.$
b) $Re(\epsilon_T) = (1.2 \pm 1.4) \cdot 10^{-3}$ $\chi^2 = 196/142 d.o.f.$
c) $Re(\epsilon_T) = (2.0 \pm 0.6) \cdot 10^{-3}$ $\chi^2 = 203/142 d.o.f.$
d) $Re(\epsilon_T) = (2.2 \pm 1.1) \cdot 10^{-3}$ $\chi^2 = 203/142 d.o.f.$

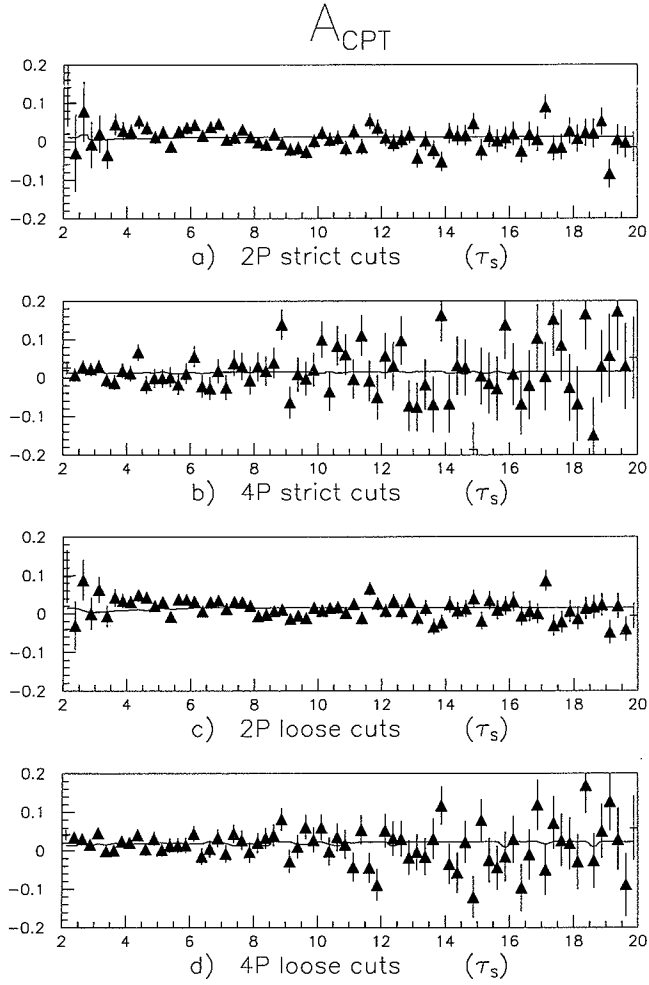

Figure 7.3: *Fit of A_{CPT}) from 2 τ_S to 20 τ_S (together with the δ asymmetry) for the 2 primary (2P) and 4 primary (4P) trigger alternatives for strict and loose cuts. The fitted line is defined according to the semileptonic rates in (2.38) and eq. (2.40) assuming $\Delta S = \Delta Q$ and $Im(\delta_{CPT}) = 0$. Note that the data is not corrected for η and since this is taken into account in the fit the level of the line is not equal to $4Re(\delta_{CPT})$. The results are:*

a) $Re(\delta_{CPT}) = (0.4 \pm 0.8) \cdot 10^{-3}$ $\chi^2 = 185/142 d.o.f.$
b) $Re(\delta_{CPT}) = (0.2 \pm 1.4) \cdot 10^{-3}$ $\chi^2 = 190/142 d.o.f.$
c) $Re(\delta_{CPT}) = (0.8 \pm 0.6) \cdot 10^{-3}$ $\chi^2 = 207/142 d.o.f.$
d) $Re(\delta_{CPT}) = (0.8 \pm 1.1) \cdot 10^{-3}$ $\chi^2 = 196/142 d.o.f.$

in 1992, P24 and P25 in 1993 while P26 took place in 1994. The order of magnitude of the number of events for the different periods is a bit less for P17 and about the same for P24-P26. There are no significant deviations of the results comparing the different data taking periods, the two trigger categories, or for the two different set of cuts. The results in Fig. 7.1 indicates a stable detector performance. Combining the results for the strict cuts we obtain $Re(\epsilon_T) = (1.6 \pm 0.7_{stat}) \cdot 10^{-3}$ and $Re(\delta_{CPT}) = (0.4 \pm 0.7_{stat}) \cdot 10^{-3}$ while for the loose cuts the combined results are $Re(\epsilon_T) = (2.1 \pm 0.6_{stat}) \cdot 10^{-3}$ and $Re(\delta_{CPT}) = (0.8 \pm 0.5_{stat}) \cdot 10^{-3}$. The statistical errors given are calculated in the fit by the function minimization and error analysis software MINUIT [101]. The results for $Re(\delta_{CPT})$ and for $Re(\epsilon_T)$ are above zero for all the cases. The combined results are statistically around 1.5 standard deviations away from zero for $Re(\delta_{CPT})$ and 3.5 standard deviations away from zero for $Re(\epsilon_T)$.

The fits to the asymmetry A_T for the overall sum of the data is shown in Fig. 7.2 for all the trigger cases. In Fig. 7.3 the same is displayed for the A_{CPT} asymmetry. The background has been taken into account in the fit and not subtracted from the data and this causes some wiggles in the fitted lines. The fits are reasonable in the sense that no systematic deviations of the data from the fitted line can be seen. On the other hand the χ^2 of the fit is not very good and the χ^2 probability generally less than 1%. There is no *apriori* reason why η should be flat in lifetime. The variation of η as a function of lifetime (Fig. 6.10) seems to be small but a dependance of the same order as the statistical errors is not unlikely. If one takes into account a variation of η by fitting different eta for different lifetime intervals the χ^2 probability increases, e.g. one η for every group of four lifetime bins (18 additional free parameters and corresponding decrease in degrees of freedom) yield a χ^2 probability over one percent for all fits. The variation of η does not have any significant impact on the result for the other fitted parameters. This is understandable since only the average η is important. We conclude that there is some dependence of η on the lifetime and this affects the χ^2 of the fit, but it does not have any impact on the fitted physics parameters.

7.2 Mass difference between K_L and K_S

The event selection and analysis is not optimized to measure the mass difference Δm between K_L and K_S. The Δm measurement serves in this context as a quality check of the data. A detailed description of the most accurate CPLEAR determination of Δm is given in [46], where it is shown that the systematic errors are almost negligible compared to the statistical ones. The value obtained for Δm fitting asymmetry (2.42) is $(0.522 \pm 0.005) \cdot 10^{10}\hbar s^{-1}$ for strict cuts. The fit is displayed in Fig. 7.4a and the χ^2 is 181 for 142 d.o.f.. The result is a bit lower than the world average [29] $(0.5333 \pm 0.0027) \cdot 10^{10}\hbar s^{-1}$ but in agreement with the most recent measurements [44, 23], which give a value for Δm of $(0.5257 \pm 0.0049) \cdot 10^{10}\hbar s^{-1}$. With loose cuts the measurement of Δm becomes uncertain because this asymmetry is sensitive to the resolution of the lifetime of the neutral kaon. This resolution gets worse for loose cuts because of the events with an extra π^0 at the primary vertex. The limited resolution will smear the lifetime distribution and the fitted value for Δm has to be corrected (upwards) for this effect. This is done using MC events by comparing the value obtained using the true kaon lifetime to the value using the measured kaon lifetime. The obtained correction is $(0.019 \cdot 10^{10})\hbar s^{-1}$. The corrected result for Δm using loose cuts (Fig. 7.4)b is $(0.520 \pm 0.005) \cdot 10^{10}\hbar s^{-1}$ for a $\chi^2 = 207/142 \quad d.o.f.$.

7.3 Systematic errors

7.3.1 Geometrical effects

We have examined the geometrical asymmetry of the detector by comparing data with reversed magnetic fields. The two data sets are referred to as M1 and M2. A test of the sensitivity of $Re(\epsilon_T)$ and $Re(\delta_{CPT})$ to geometrical asymmetries of the detector is the change of these parameters when the magnetic field changes. Since for events with two primaries there is no dependence on M1/M2 there is no systematic effect from geometry. For events with four primaries there is, however, a dependence of the parameters of the order of one percent. The same variation is seen in the Monte Carlo. After mixing equal amounts of M1 and M2 in the

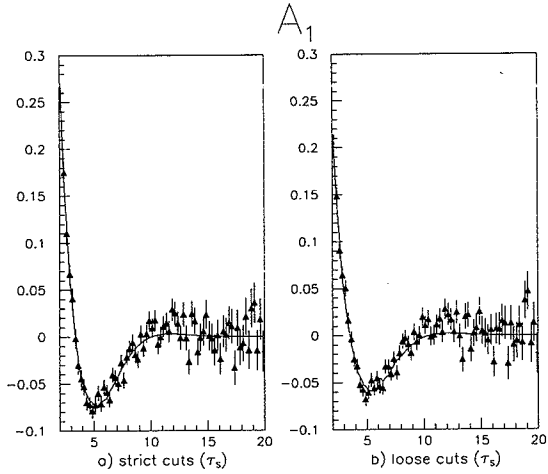

Figure 7.4: *Fit of A_1 asymmetry from 2 τ_S to 20 τ_S (together with the δ asymmetry) for strict and loose cuts with η and Δm as free parameters. There is only a weak correlation between η and Δm. The fitted line is defined according to the semileptonic rates in (2.38) and eq. (2.42) assuming $\Delta S = \Delta Q$. The results are:*
a) $\Delta m = (0.524 \pm 0.005) \cdot 10^{10} \hbar s^{-1} \quad \chi^2 = 181/142 d.o.f.$
b) $\Delta m = (0.520 \pm 0.005) \cdot 10^{10} \hbar s^{-1} \quad \chi^2 = 207/142 d.o.f.$

Monte Carlo the residual effect is compatible with zero.

The best check is to compare the results for asymmetries of single track curvature. This means for A_T to fit the asymmetry using M1 data for the first term in eq. (2.39) and M2 data for the second term. One could then do the inverse and use M2 data for the first term and M1 data for the second term. If there is any remaining geometrical residual effects it should show up as a systematic difference in the results fitting the asymmetries for the two curvatures. In Fig. 7.5 the results for the different curvatures and different periods are shown for the loose cuts. There is no visible systematic differences for the two curvatures and we conclude that any remaining residual geometric effect is negligible.

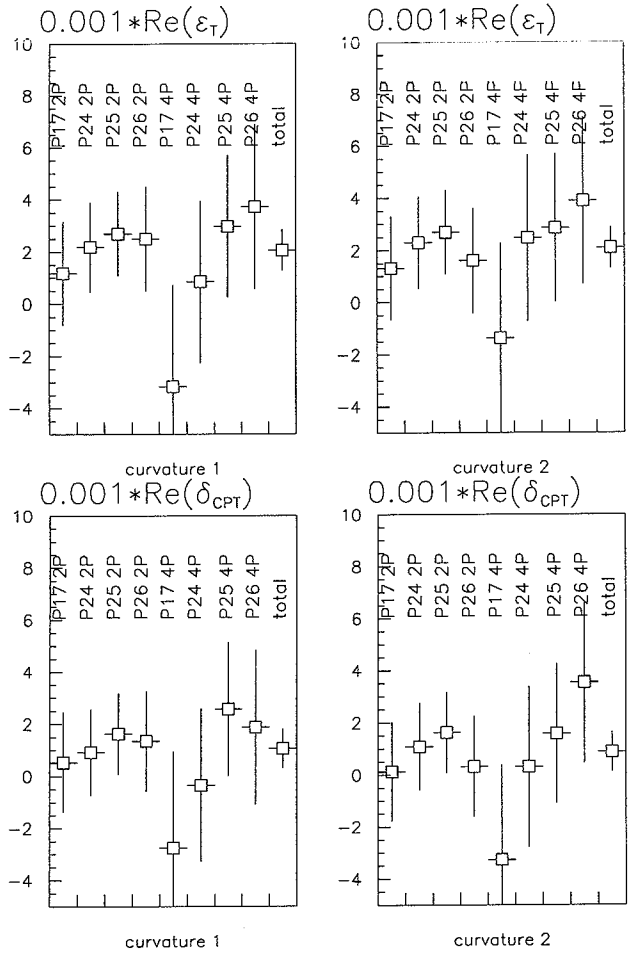

Figure 7.5: *Results for A_T and A_{CPT} in terms of $Re(\epsilon_T)$ and $Re(\delta CPT)$. The results are plotted for curvature 1 and curvature 2 (as defined in the text) for the 2 primary (2P) and 4 primary (4P) trigger alternatives for loose cuts and different data taking periods. The data taking periods are from P17 in (1992) to P26 in (1994)*

7.3.2 The normalization of K^0 versus $\overline{K^0}$

For each bin in the LUT used for the $K^0/\overline{K^0}$ normalization there is a statistical error e_{norm} corresponding to the number of events used to build the ratio in the LUT. This error has been taken into account summing over all bins and putting a weight that depends on the statistical error e_{bin} in each bin of the LUT and the number of times n a particular bin was used.

$$e^2_{norm} = \sum_{bin=1}^{1728} = n^2_{bin} \cdot e^2_{bin} \tag{7.1}$$

The error e_{norm} is taken into account as a systematic error adding up to $0.20 \cdot 10^{-3}$ for $Re(\epsilon_T)$. The effect of the binning of the LUT is negligible.

7.3.3 Uncertainty of the world average value for δ

The precision of the world average value for δ [29] is ± 0.00012 for K_L. The uncertainty of δ translates into a systematic error in $Re(\delta_{CPT})$ and $Re(\epsilon_T)$ of $1 \cdot 10^{-5}$

7.3.4 Background uncertainty

The flat asymmetries 2.39 and 2.40 are not very sensitive to the absolute value of the background. Variation of the background with as much as $\pm 10\%$ results in a negligible change in $Re(\epsilon_T)$ and $Re(\delta_{CPT})$. On the

	2 primary	4 primary	total
strict cuts	$0.10 \cdot 10^{-3}$	$0.18 \cdot 10^{-3}$	$0.12 \cdot 10^{-3}$
loose cuts	$0.07 \cdot 10^{-3}$	$0.38 \cdot 10^{-3}$	$0.15 \cdot 10^{-3}$

Table 7.1: *Systematic error from possible asymmetry in the background*

other hand there is a sensitivity to an asymmetric background, where a different number of $\pi^+\pi^-$ is identified as $e^+\pi^-$ than is identified as π^+e^-. There is no sign of such an asymmetry in data or MC. A conservative

upper limit of a possible asymmetry is 10% for strict cuts and 7% for loose cuts. These limits could be reduced with an increase of the number of generated MC events in the $\pi^{\pm}\pi^{\mp}$ decay channel of the neutral kaons. Since very few events survive the cuts it is very CPU demanding to simulate the background. The resulting uncertainty for $Re(\epsilon_T)$ and $Re(\delta_{CPT})$ is summarized in table 7.1

7.4 Conclusion

Since 1992 the CPLEAR detector has been working stable and reliable for data taking periods that altogether total almost one year. The PID sub detector that is discussed in detail in this thesis has displayed a stable $\pi^{\pm}$ rejection efficiency.

Almost one million semileptonic events have been selected and analyzed using neural networks. The final results for the T-violation parameter $Re(\epsilon_T)$ is $(2.1 \pm 0.6_{stat} \pm 0.3_{sys})10^{-3}$, corresponding to a deviation from zero in the A_T asymmetry of $(8.6 \pm 2.2_{stat} \pm 1.0_{sys})10^{-3}$. This is more than three standard deviations from zero and is the first direct measurement of T-violation. The result for $Re(\epsilon_T)$ can be compared to the value $1.61 \cdot 10^{-3}$ for $Re(\epsilon_L)$ [29]. As a cross check the value determined for $Re(\delta_{CPT})$ is $(0.8 \pm 0.5_{stat} \pm 0.3_{sys}) \cdot 10^{-3}$. The systematic error almost exclusively arises from uncertainty in the normalization of the flux of K^0 versus $\overline{K^0}$ and from a possible asymmetry in the background. We conclude that T is indeed violated in the neutral Kaon system while the data does not reveal any evidence of CPT violation.

Acknowledgements

First I would like to thank Prof Per Carlson, who has, as head of the institution for particle physics and instrumentation section at KTH, secured the financial support for my participation in the CLPEAR experiment at CERN. Over the years he made many useful suggestions for my physics analysis. I also appreciate that he gave me a lot of freedom to follow my own paths and test my own ideas.

During the last two years of semileptonic analysis Doc Kerstin Jon-And has supervised my work. She has helped me out several times when I was stuck and was always willing to answer my questions, no matter how simple or difficult. It has been an outstanding intellectual experience to work with Kerstin.

During the course of the experiment I have also had the great opportunity to work with Prof Hans-Jürg Gerber and Prof Ludwig Tauscher, two physicists of the old school. With Prof Gerber I shared an intense effort to solve problems with the Cherenkov liquid and I learned a lot from his broad knowledge in physics. Prof Ludwig Tauscher taught me about the annihilation process and the art of meson spectroscopy.

The leader of the semileptonic analysis, Dr Marc Dejardin, has been in charge of the tremendous work of filtering and preprocessing the semileptonic data. He has continuously supported me with many good pieces of advice. Doc Tatsuya Nakada has guided me through the phenomenology of the neutral kaon system and patiently answered my questions. I am grateful to him for proofreading chapters 1 and 2.

In CPLEAR I would like to thank our spokesperson Prof Noulis Pavlopoulos together with Prof Alcibiades Apostolakis, Frederic Blanc, Dr Phil Bloch, Andy Cody, Michael Dröge, Dr João Carvalho, Maxwell Chertok, Dr Christos Eleftheriadis, Prof Maria Fidecaro, Dr David Francis, Robert Kreuger, Dr Anastasios Liolios, Emanuel Machado, Prof Jim Miller, Dr Francois Montanet, Dr Marko Mikuž, Igor Mandić, Dr Antonio Onofre, Dr René Rickenbach, Prof Lee Roberts, Dr Thomas Ruf, Dr Andreas Schopper, Dr Catherine Thibault, Dr Christos Touramanis, Dr Sotirios Vlachos, Dr Peter Weber, Othmar Wigger, Marčin Wolter, David Zimmerman and many others who are not mentioned for fruitful discussions and nice company. At CERN I also had valuable discussions with Georg Lenzen concerning Cherenkov radiators and he helped me with transmis-

sion tests of C_6F_{14}.

In the Stockholm group I had the pleasure to work with Dr Kåre Jansson and Dr Apollo Go. During the first years as a PhD student I shared analysis work concerning spectroscopy with Kåre and I have used his latex skeleton for my thesis. The last years I have worked extensively with Apollo and he has helped me with making several figures and the normalization for the primary vertex. I have knocked on the door to his office many times to discuss physics. Not the least important, Kåre has taught me which French restaurants to visit and Apollo has taught me to appreciate Chinese food.

During most of the time I have had the enjoyment of sharing an office with Jesper Söderqvist. This has resulted in a sailing boat for me for one thing. In addition we have organized several activities for the students at KTH as well as collaboration with industry together. No one compares to Jesper when it comes to organizing activities!

In what have been the department for particle physics and instrumentation at KTH the last years I would also like to mention Lars-Ove Eek, Tom and Kerstin Francke, Christer Fuglesang, Thomas Lindblad, Clark Lindsey, Bengt Lund-Jensen, Nicklas Weber and I also had the joy of getting to know the two diploma workers Jörgen Sjölin and Mikael Timm. Doc Tom Francke provided the ignition for me to start working in particle physics and I remember with delight several dinners with Tom and Kerstin Francke in their house in Thoiry. Clark Lindsey has made the tremendous work of proofreading the whole thesis and together with Thomas Lindblad taught me about neural networks. Sten Leven has helped me with a figure. From KTH I also want to mention Karl-Erik Bergkvist, Bo Cederwall, Joakim Cederkäll, Peter Erman, Arne Johnson, Andras Kerek, Karl-Axel Pettersson, Ulf Ringström, Elisabeth Rachlew, Göran Sundström, Göran Tranströmer, Ramon Wyss and Klaus-Dieter Zastrow. I also want to thank Carl-Gunnar Lindén and Jan Michelson at the Manne Siegbahn Laboratory for computer support as well as the the administration at KTH Frescati for helping me with practical matters.

Most of all I am, of course, indebted to my wife Maria.

Bibliography

[1] E. Noether, Nachr. Ges. Wiss. Göttingen (1918)171

[2] L. Adiels et al., Proposal for the experiment PS195/CPLEAR CERN PSCC/85-6 P82 (1985), PSCC/85-30 P82 (1985), PSCC/86-34 M263 (1986), PSCC/87-14 M272 (1987)

[3] E. Gabathuler and P. Pavlopoulos, proc. of the "Workshop on physics at LEAR", ed. U. Gastaldi and R. Klapich, Plenum Publisher (1982)747

[4] T.D. Lee and C.N. Yang, Phys. Rev. **104**(1956)254

[5] C.S. Wu et al., Phys. Rev. **105**(1957)1413

[6] G. Ekspong, private communications

[7] J.H. Christenson et al., Phys. Rev. Lett. **13**(1964)138

[8] C. Geweniger et al., Phys. Lett. B **48**(1974)483

[9] G. Lüders, Kgl. Danske Videnskab. Selskab, Mat.-fys. Medd. **28**(1954)

[10] J. Schwinger, Phys. Rev. **91**(1953)720

[11] J. Schwinger, Phys. Rev. **94**(1953)1366

[12] J. Ellis, N.E. Mavromatos and D.V. Nanopoulos, Phys. Lett. B **293**(1992)37

[13] R. Adler et al. (the CPLEAR collaboration) and J. Ellis, J.L. Lopez, N.E. Mavromatos, D.V. Nanopoulos, Phys. Lett. B **364**(1995)239

[14] P. Huet and M.E. Peskin, Nucl. Phys. B **434**(1995)3

[15] T. Nakada, Proc. of the "International Symposium on Lepton-Photon Interactions at High Energy Physics", ed. P. Drell and D. Rubin, Ithaca, USA, (1993)

[16] L. Wolfenstein, Ann. Rev. Nucl. Part. Sci. **36**(1986)137

[17] J. Cronin, Rev. Mod. Phys. **53**(1981)373

[18] C. Jarlskog, Phys. Rev. Lett. **55**(1985)1039

[19] M. Kobayashi and T. Maskawa, Prog. Theor. Phys. Japan **49**(1973)652

[20] L. Wolfenstein, Phys. Rev. Lett. **13**(1964)562

[21] G. Chardin, Nucl. Phys. A **558**(1993)477

[22] H. Burkhardt et al. (the NA31 collaboration), Phys. Lett. B **206**(1988)169

[23] L.K. Gibbons et al. (the E731 collaboration), Phys. Rev. Lett. **70**(1993)1199

[24] G.D. Barr et al., Proposal for the experiment NA48 CERN/SPSC/90-22 SPSC/P253 (1990)
G.D. Barr et al., Phys. Lett. B **317**(1993)233

[25] K. Arisaka et al., KTeV design report, FERMILAB FN 580(1992)

[26] B. Winstein and L. Wolfenstein, Rev. Mod. Phys. **65**(1993)1113

[27] F. Abe et al. (the CDF collaboration), FERMILAB-PUB-95/022-E (1995)

[28] A.J. Buras, M. Lamin and M.E. Lautenbacher, Nucl. Phys. B **408**(1993)209

[29] Particle Data Group, Phys. Rev. D **50**(1994)

[30] T. Nakada, lecture notes, ETH Zürich (1994)

[31] P.K. Kabir, "The CP Puzzle", Academic Press (1968)

[32] R.G. Sachs, "The Physics of Time Reversal", University of Chicago Press (1987)

[33] L. Lavoura, Ann. of Phys. **207**(1991)428

[34] E.P. Wigner, Nachr. Ges. Wiss. Göttingen Math-Physik K1 **32**(1932)546

[35] E.P. Wigner, "Group Theory", Academic Press, New York (1959)

[36] G.D. Rochester and C.C. Butler, Nature Lond. **160**(1947)855

[37] M. Gell-Mann and A. Pais, Phys. Rev. **97**(1955)1387

[38] V.F. Weisskopf and E.P. Wigner, Z. Phys. **63**(1930)54

[39] V.F. Weisskopf and E.P. Wigner, Z. Phys. **65**(1930)18

[40] J.S. Bell and J. Steinberger, Proc. of the "International Conference on Elementary Particles", Oxford, UK, (1965)195

[41] M. Karlsson, PhD thesis Princeton University (1990)

[42] T.J. Devlin and J.O. Dickey, Rev. Mod. Phys. **51**(1979)237

[43] D. Fournier (the NA31 collaboration), Proc. of the "International Symposium on Lepton-Photon Interactions at High Energies", ed. M. Riordan, Stanford, USA (1989)
R. Carosi et al. (the NA31 collaboration), Phys. Lett. B **237**(1990)303

[44] B. Schwingenheuer et al. (the E773 collaboration), Phys. Rev. Lett. **74**(1995)4376

[45] R. Adler et al. (the CPLEAR Collaboration), Phys. Lett. B **363**(1995)243

[46] R. Adler et al. (the CPLEAR Collaboration), Phys. Lett. B **363**(1995)237

[47] R. Adler et al. (the CPLEAR collaboration), "A new determination of the K_L-K_S mass difference and the phase of the CP violation parameter η_{+-} from an evaluation of experimental data", CERN-PPE/95-112, Submitted to Z. Phys. C, with another title: "Precision determination of the K_L-K_S mass difference and the phase of the CP violation parameter η_{+-} from a correlation analysis of different experiments"

[48] K. Jon-And, Nucl. Phys. A, **558**(1993)449

[49] R. Adler et al. (the CPLEAR Collaboration), "A direct measurement of T-violation", To be submitted to Phys. Lett. B (in preparation)

[50] P.K. Kabir, Phys. Rev. **D2**(1970)540
A. Aharony, Lett. Nuovo Cim. **3**(1970)791
and implicitly by
R.G. Sachs, Phys. Rev. **129**(1963)2280

[51] J. Carvalho, PhD thesis University of Liverpool (1994)

[52] P. Kokkas (the CPLEAR collaboration), Proc. of the "Four seas conference", Trieste, Italy, (1995)

[53] R. Adler et al., "The CPLEAR detector at CERN", to be submitted to Nucl. Instr. Meth. A

[54] V. Fitch et al., Phys. Rev. Lett. **1573**(1965)

[55] C. Guyon, CERN/EP/PS195/MBL/001 (1988)

[56] R. Adler et al., Nucl. Instr. Meth. A **321**(1992)458

[57] M. van den Putte et al., IEEE Trans. Nucl. Sci. **37**(1990)53

[58] R. Kreuger, PhD thesis Delft Tech. Univ. in preparation

[59] C. Amsler and F. Myhrer, Ann. Rev. Nucl. Part. Sci. **41**(1991)219

[60] F. Sauli CERN Report 77-09 (1977) and
Ch. Bula, PhD thesis ETH Zürich (1992)

[61] M. Dejardin, PhD thesis, Universite de Paris 7 (1992)

[62] E. Cawley, PhD thesis, University of Liverpool (1995)

[63] A. Go et al., Nucl. Instr. Meth. A **333**(1993)513

[64] M. Kreciejewski et al., Nucl. Instr. Meth. A **301**(1991)424

[65] R. Adler et al. (the CPLEAR collaboration), "First observation of a particle-antiparticle asymmetry in the decay of neutral kaons into $\pi^0\pi^0$", CERN-PPE/95-149, to appear in Z. Phys. C (1996)

[66] S. Vlachos, PhD thesis University of Liverpool (1992)

[67] A. Angelopoulos et al., Nucl. Instr. Meth. A **311**(1992)78

[68] Valet Plus System, CERN users manual

[69] G. Marel, notes from CPLEAR tuesday meeting (1994)

[70] P. Pavlopoulos and S. Vlachos, Nucl. Instr. Meth. A **324** (1993)320

[71] M. Danielsson et al., Nucl. Instr. Meth. A **350**(1994)322

[72] P. Carlson, Nucl. Instr. Meth. A **166**(1979)425

[73] T. Ekelöf, Proc. of the "12th SLAC Summer institute on particle physics", ed. P. McDonough, Stanford, USA (1984)244

[74] T.L. Francke, PhD thesis KTH Stockholm (1991)

[75] E.G. Anassontzis et al., IEEE Trans. Nucl. Sci. **38**(1991)417

[76] M. Cavalli-Sforza et al., IEEE Trans. Nucl. Sci. **37**(1991)1132

[77] J. Baechler et al., Nucl. Instr. Meth. A **343**(1994)213

[78] "The fluorinert liquids", data sheets from 3M Belgium

[79] G. Lenzen et al., Nucl. Instr. Meth. A **343**(1994)268

[80] L.D. Rozenberg, "Physical principles of ultrasonic technology", Vol. 1, Plenum Press (1973)

[81] P.W. Atkins, "Physical Chemistry", third edition, Oxford University Press (1986)

[82] P. Bloch, "On pionic background rejection", CPLEAR internal note, CP/NORM/6

[83] K. Jansson, PhD thesis KTH Stockholm (1993)

[84] R.A. Holroyd et al., Nucl. Instr. Meth. A **261**(1987)78

[85] K. Watanabe, E.C.Y. Inn, J. Zelikoff, J. Chem. Phys. **21**(1953)1026
K. Watanabe, E.C.Y. Inn, J. Zelikoff, J. Chem. Phys. **20**(1952)1969
R. Ladenburg and C.C. van Voorhis, Phys. Rev. **43**(1933)315
K. Watanabe, Advan. Geophys. **5**(1958)153
K. Watanabe and F.F. Marmo, J. Chem. Phys. **25**(1956)965
E.G. Schneider, J. Chem. Phys. **5**(1937)106
Y. Tanaka, J. Chem. Phys. **20**(1952)1728

[86] M. Danielsson and H.J. Gerber, Nucl. Instr. Meth. A **334**(1993)339

[87] G. Lenzen, private communications

[88] P. Gumplinger, "CPGEANT user guide", CPLEAR offline note (1989)

[89] R. Brun et al., "GEANT user guide", CERN DD/EE/84-1 (1986)

[90] A. Ealet et al., "NHPLIB user guide", CPLEAR offline note (1991)

[91] D. Rumelhart and J. McClelland, "Parallel Distributed Processing", MIT press 1986

[92] A.N. Kolmogorov, "On the Representation of Continuous Functions of Many Variables by Superposition of One Variable and Addition" (in russian), Dokl. Akad. Nauk. USSR **114**(1957)953

[93] L. Lönnblad et al., Phys. Rev. Lett. **65**(1990)1321

[94] K. Hultqvist, R. Jacobson and K.E. Johansson, Nucl. Instr. Meth. A **364**(1995)193

[95] B. Denby et al., Nucl. Instr. Meth. A **335**(1993)296

[96] C.S. Lindsey, Proc. of the "3rd Workshop on Neural Networks: From Biology to High Energy Physics", Isola d'Elba, Italy, (1994)

[97] "Electrically Trainable Analog Neural Network 80170NX", data sheet from Intel Corp., Santa Clara, USA (1993)

[98] M. Dejardin, "Electron-Pion Separation using Neural Network Technique with PID Information", CPLEAR internal report CP/SW/043 (1993)

[99] J.M. Zurada, "Artificial Neural Systems", West Publ. Co. (1992)

[100] A. Go, PhD Thesis Boston University (1994)

[101] F. James and M. Roos, "MINUIT Function Minimization and Error Analysis", CERN Program Library Entry D506, version 2.1 (1992)

Papers to which the author of this thesis is either author or co-author are [13, 45, 46, 47, 49, 53, 65, 71] and [86]. The following works by this author is not included in the thesis:

"Deduction of central plasma parameters from line-of-sight averaged spectroscopic observations"
K.-D. Zastrow, H.W. Morsi, M. Danielsson, M.G. von Hellermann, E. Källne, W. Mandl and H.P. Summers
J. Appl. Phys. Vol, **70**(1991)6732

"On comparison of spectroscopically deduced central ion temperatures and plasma rotation at JET"
M. Danielsson, M.G. von Hellermann, E. Källne, W. Mandl, H.W. Morsi, H.P. Summers and K.-D. Zastrow
Rev. Sci. Instrum., **63**(1992)2241

"Predissociation effects in the $A^2\Delta$ and $B^2\Sigma^-$ states of CD"
M. Danielsson, P. Erman, A. Hishikawa, M. Larsson, E. Rachlew-Källne and G. Sundström
J. Chem. Phys. Vol., **98**(1993)9405

"A hardware neural network for on-line particle identification"
M. Danielsson, A. Go, K. Jon-And, Th. Lindblad, E. Machado and M. Timm
Nucl. Instr. Meth. A, **350**(1994)322

"A straightforward exercise demonstrating Heisenberg's uncertainty principle"
M. Danielsson, J. Söderqvist and P. Carlson
Eur. J. Phys., **16**(1994)97

"Inclusive measurement of $\bar{p}$ annihilation at rest in gaseous hydrogen to final states containing ρ and f_2"
P. Carlson, M. Danielsson, K. Jansson and L. Tauscher
CPLEAR internal report, later published with
R. Adler et al. (the CPLEAR Collaboration, 105 co-authors)
Z. Phys. C, **65**(1995)199

List of Figures

List of Tables